



Water Resources Research®

RESEARCH ARTICLE

10.1029/2022WR034302

Modeling the Transport and Retention of Nanoparticles in a Single Partially Saturated Pore in Soil

J. Jayaraj¹, N. Seetha¹ , and S. Majid Hassanizadeh^{1,2,3} 

¹Department of Civil Engineering, Indian Institute of Technology Hyderabad, Sangareddy, India, ²Stuttgart Center for Simulation Science (SIMTECH), Integrated Research Training Group SFB 1313, Stuttgart University, Stuttgart, Germany,

³Department of Earth Sciences, Utrecht University, Utrecht, The Netherlands

Key Points:

- A novel formulation for particle diffusive transport from air-water interface to contact region
- Parameters describing geometry, flow, and hydrophobic energy govern particle retention at interfaces
- Developed algebraic relationships between 1D-averaged deposition rate coefficients at interfaces vis-à-vis various pore-scale parameters

Supporting Information:

Supporting Information may be found in the online version of this article.

Correspondence to:

N. Seetha,
seetha@ce.iith.ac.in

Citation:

Jayaraj, J., Seetha, N., & Hassanizadeh, S. M. (2023). Modeling the transport and retention of nanoparticles in a single partially saturated pore in soil. *Water Resources Research*, 59, e2022WR034302. <https://doi.org/10.1029/2022WR034302>

Received 8 JAN 2023

Accepted 12 MAY 2023

Author Contributions:

Conceptualization: N. Seetha, S. Majid Hassanizadeh

Formal analysis: J. Jayaraj

Funding acquisition: N. Seetha

Investigation: J. Jayaraj

Methodology: J. Jayaraj, N. Seetha, S. Majid Hassanizadeh

Software: J. Jayaraj

Supervision: N. Seetha

Writing – original draft: J. Jayaraj

Writing – review & editing: N. Seetha, S. Majid Hassanizadeh

Software: J. Jayaraj

Abstract Pore-network models are powerful tools for studying particle transport in complex porous media, and investigating the role of interfaces in their fate. The first step in simulating particle transport using pore-network models is to quantitatively describe particle transport in a single pore, and obtain relationships between pore-averaged deposition rate coefficients and various pore-scale parameters. So, in this study, a three-dimensional (3D) mathematical model is developed to simulate the transport and retention of nanoparticles within a single partially saturated pore with an angular cross-section. The model accounts for particle deposition at solid-water interfaces (SWIs), air-water interfaces (AWIs), and air-water-solid (AWS) contact regions. We provide a novel formulation for particle diffusive transport from AWI to AWS, where particles are assumed to be retained irreversibly by capillary forces. The model involves 12 dimensionless parameters representing various physicochemical conditions. The 3D model results are averaged over the pore cross-section and then fitted to breakthrough curves from one-dimensional (1D) advection-dispersion-sorption equations with three-site kinetics to estimate 1D-averaged deposition rate coefficients at interfaces. We find that half-corner angle, particle size, radius of curvature of AWI, and mean flow velocity have a significant effect on those coefficients. In contrast, chemical parameters such as ionic strength and surface potentials of particles and interfaces have negligible effects. AWS is found to be the major retention site for particles, especially for hydrophobic particles. We develop algebraic relationships between 1D-averaged deposition rate coefficients at interfaces vis-à-vis various pore-scale parameters. These relationships are needed for pore-network models to upscale nanoparticle transport to continuum scale.

1. Introduction

Due to their tuneable surface properties, engineered nanoparticles are widely used in various consumer products, industries, and biomedical fields (Grillo et al., 2015; Kessler, 2011; Rudramurthy & Swamy, 2018). This results in their inevitable release into wastewater. Traditional municipal wastewater treatment plants are not capable of removing engineered nanoparticles (Chauque et al., 2014; Khan et al., 2021). Hence, engineered nanoparticles, along with active bio-nanoparticles, such as viruses, may enter the subsurface through land application of treated wastewater, and wastewater disposal to surface water bodies, and eventually enter the subsurface. Before reaching groundwater, they get transported through the vadose zone, where a fraction of the infiltrated particles is retained at grain surfaces (also called solid-water interface, SWI), air-water interface (AWI), and air-water-solid (AWS) contact region (Gao et al., 2008; Sang et al., 2013; Sirivithayapakorn & Keller, 2003; Wan et al., 1994; Wan & Wilson, 1994; Zevi et al., 2005, 2009). However, the retained particles can also be released back into the bulk water due to temporal variations in flow and chemistry (El-Farhan et al., 2000; Gomez-Suarez et al., 1999a, 1999b, 2000, 2001; Kaplan et al., 1993; Ryan et al., 1998). The particles which are not retained in the vadose zone move down and contaminate the groundwater. Hence, it is important to study the transport mechanisms of nanoparticles in partially saturated porous media to evaluate the potential for the groundwater contamination.

A vast majority of literature on particle transport in porous media pertains to saturated conditions (Bradford & Bettahar, 2005; Foppen et al., 2005; Li et al., 2004, 2005; Redman et al., 2001; Schijven & Hassanizadeh, 2000; Tong et al., 2005; Tufenkji & Elimelech, 2004). However, there are only a few formulas for estimating particle deposition rate coefficients in saturated porous media as a function of various physicochemical parameters. This includes the theoretical models such as (a) colloid filtration theory which estimates particle attachment rate coefficient under favorable conditions for deposition (Logan et al., 1995; Schijven & Hassanizadeh, 2000; Yao et al., 1971), and (b) the model of Seetha et al. (2017) which predicts nanoparticle attachment and detachment

rate coefficients under unfavorable conditions. There are also a few empirical models, including (a) the model of Krishna and Seetha (2022), which predicts the deposition rate coefficient of viruses, bacteria, titanium dioxide nanoparticles, graphene oxide nanoparticles, silver nanoparticles, and carboxylate-modified latex microspheres, and (b) models of Bai and Tien (1999), Sadeghi et al. (2011), and Y. Park et al. (2012) which predict the sticking efficiency of latex particles, bacteriophage PRD1, and *Cryptosporidium parvum* Oocysts, respectively. Comparatively, few studies have focused on particle transport in partially saturated porous media (Chen & Flury, 2005; L. Chen et al., 2005, 2008, 2010, 2012; Saiers & Lenhart, 2003; Saiers et al., 2003; Schafer, Harms, et al., 1998; Schafer, Ustohal, et al., 1998; Wan & Tokunaga, 1997; Wan & Wilson, 1994; Wan et al., 1994). Moreover, formulas to estimate colloid deposition parameters under partially saturated conditions do not exist.

Colloid retention in a porous medium has been observed to be greater under partially saturated conditions than under fully saturated conditions due to the presence of multiple retention sites, including SWI, AWI, and AWS (Crist et al., 2004, 2005; Wan et al., 1994; Wan & Wilson, 1994; Zevi et al., 2005; Zhang et al., 2013, 2014), and thin liquid films (Cherrey et al., 2003; Crist et al., 2004, 2005; Saiers & Lenhart, 2003; Schafer, Harms, et al., 1998; Torkzaban et al., 2006; Wan & Tokunaga, 1997; Zevi et al., 2005). Colloid transport in partially saturated porous media depends on geometrical parameters, such as pore-size distribution, pore shape, particle size, and particle shape (Wan & Tokunaga, 1997; Zhuang et al., 2005), on chemical parameters, such as solution ionic strength, pH, and surface properties of grains and particles (Chen & Flury, 2005; Choi & Corapcioglu, 1997; Torkzaban et al., 2008), on flow velocity (Knappenberger et al., 2014; Wan & Tokunaga, 1997), and on degree of saturation (Knappenberger et al., 2014; Saiers et al., 2003; Saiers & Lenhart, 2003; Torkzaban et al., 2006; Wan & Tokunaga, 1997). Particle retention in porous media is found to increase with decreasing degree of saturation due to the availability of more AWIs for deposition and straining in thin films that form at low saturation (Schafer, Harms, et al., 1998; Schafer, Ustohal, et al., 1998; Wan & Wilson, 1994; Wan & Tokunaga, 1997; Zevi et al., 2005). However, the interplay among various mechanisms and their relative importance in retaining particles with change in degree of saturation is not clear. For example, many studies have concluded retention at AWI to be the most important mechanism and the contribution of SWI in particle retention to be negligible (Cherrey et al., 2003; Schafer, Harms, et al., 1998; Torkzaban et al., 2008; Wan & Tokunaga, 1997; Wan & Wilson, 1994). It is also suggested that the retention at AWI is due to the capillary force exerted on the attached particles (Kralchevsky & Nagayama, 2001; Sang et al., 2013). Several researchers have found that the capillary force acting on particles at AWI is orders of magnitude greater than the van der Waals and electrostatic forces between particles and AWI (Butt et al., 2005; Gao et al., 2008; Ishida, 2007; Shang et al., 2008; Sharma et al., 2008). Moreover, particles have been observed to be retained irreversibly at AWI with the retention being larger for hydrophobic colloids than hydrophilic colloids (Schafer, 1998a, 1998b; Wan & Wilson, 1994; Wan et al., 1994). This is due to a large negative interfacial free energy change associated with transferring a fully immersed hydrophobic particle from bulk solution to the AWI, which is an energetically favorable process (Abdel-Fattaha & El-Genk, 1998a, 1998b; Flury & Aramrak, 2017). Saiers and Lenhart (2003) and Lenhart and Saiers (2002) reported that the dominant retention mechanism changes from film straining to AWI attachment to SWI attachment with increasing degree of saturation. Saiers and Lenhart (2003a) found a similar transition in the deposition mechanism of silica colloids in partially saturated porous media with increasing ionic strength of the background solution. At lower moisture contents, film straining efficiency has been observed to increase with decreasing grain size and increasing colloid size (Wan and Tokunaga, 1997). In contrast to the above observations on the importance of AWI on particle retention, many other studies have later observed that the retention at AWS to be the most important mechanism, and the contribution by AWI for particle retention to be negligible due to the charge similarity between particles and AWI (Chen & Flury, 2005; Crist et al., 2004, 2005; Gao et al., 2008; Steenhuis et al., 2006; Zevi et al., 2005). Water at AWI has been found to be mobile and particles at AWI have been observed to undergo Brownian motion and rotation (Gehring & Fischer, 2011; Manoharan, 2015; Radoev et al., 1992; Stocco et al., 2019; Tan et al., 2009; Toro-Mendoza et al., 2017). This helps with the particles at AWI to diffuse or advect to AWS, where they get pinned by capillary forces (Bradford & Saeed, 2008; Flury & Aramrak, 2017; Kralchevsky & Nagayama, 2001; Sang et al., 2013; Xu et al., 2016). Also, particles from the aqueous phase can get strained directly at AWS.

Saiers and Lenhart (2003) observed that as ionic strength increases, retention of colloids at AWI and SWI increases. Similar observation was made by Zhuang et al. (2007), where they observed greater mobilization of colloidal particles at low ionic strengths than at high ionic strengths. However, this is contradictory to the observations of Bridge et al. (2007), who found significant attachment of colloids to AWI to happen only at low ionic strengths when the attachment to SWI is negligible. This is in line with the findings of Zevi et al. (2009), who

observed lesser retention of particles at AWS with increasing ionic strength as attachment to SWI becomes the dominant retention mechanism. Lazouskaya and Jin (2008) and Zhang et al. (2014b) observed greater retention of hydrophobic than hydrophilic particles at AWI. This is supported by the measurements using atomic force microscopy, which has shown that hydrophobic particles are attracted toward AWI and hydrophilic particles are repelled from AWI (Butt, 1994; Ducker et al., 1994; Fielden et al., 1996; Ishida, 2007). Schafer, Harms, et al. (1998) and Schafer, Ustohal, et al. (1998) observed greater retention of hydrophilic bacteria with increasing ionic strength in partially saturated porous media. But, the retention of hydrophobic bacteria was found to be not affected by variations in ionic strength (Mitropoulou et al., 2013; Torkzaban et al., 2008; Zevi et al., 2009). Colloid transport behavior also depends on the wetting history of the soil, and the colloids retained during drainage may get rapidly remobilized back into the pore water during imbibition (Crist et al., 2005; Gao et al., 2004). Colloid remobilization was found to increase with increasing velocity of AWI (Saiers et al., 2003; Zhang et al., 2013).

The above-mentioned studies under partially saturated conditions each focused on the effect of a single parameter on colloid retention and remobilization (e.g., degree of saturation, hydrophobicity of colloids, flow velocity, or ionic strength). However, one would expect a nonlinear effect of combination of these parameters on the fate of colloids. To the best of our knowledge, colloid transport and retention in partially saturated porous media while varying a wide range of physicochemical conditions has not been explored yet. Also, the interplay of the role of various retention sites on colloid attachment under different physicochemical conditions has not been understood completely. Mathematical modelling offers the advantage of studying the transport behavior of particles under a wide range of physicochemical conditions which is otherwise difficult through experiments. The smallest scale in porous media that can be studied to understand the flow and transport behavior is that of a single pore. Pore-scale modelling, and the subsequent upscaling to continuum scale using a pore-network model, offers the advantage of studying the effect of various pore-scale parameters on particle deposition behavior at the continuum scale, and to identify the dominant retention mechanisms under various physicochemical conditions. This in turn helps to develop formulas to estimate colloid deposition parameters at continuum scale in terms of various physicochemical parameters.

The goal of this study is to find algebraic relationships for average mass transfer rate coefficients governing the fate of nanocolloids transported within a single pore. We have done this in two steps. In the first step, we have developed a three-dimensional (3D) mathematical model to simulate the transport of nano-sized particles in a single partially saturated soil capillary. We assume the pore to be a parallelepiped with an angular cross section. We consider situations where the water saturation is low such that the whole pore cross-section is not filled. As we assume the pore wall to be hydrophilic, water occupies the pore corners. Due to symmetry, we only need to consider a half-corner region of the pore corner for our simulations. First, steady-state fluid flow is simulated by solving Stokes and continuity equations. Then, transient particle transport is simulated by solving advection-diffusion equation in the bulk with terms for first-order deposition on SWI and AWI. We have proposed a novel mathematical formulation for simulating nanoparticle deposition at AWS. The model consists of 12 dimensionless parameters representing various physicochemical system properties. The solution of the set of 3D equations results in 3D fields of concentrations in bulk phase and in adsorbed form.

In the second step, the pore-scale results are averaged over the water-wet cross-section of the pore. This results in one-dimensional (1D) fields of averaged concentrations in bulk phase and in adsorbed form. These results are fitted to the solution of a 1D advection-dispersion-sorption equation with three kinetic sites of adsorption to SWI, AWI, and AWS. The fitting results in a large data set of values of averaged deposition rate coefficients for a wide range of chemical, hydraulic, and geometrical conditions. Using this data set, a power-law relationship is proposed between 1D averaged deposition rate coefficients at SWI, AWI, and AWS and the various pore-scale parameters. This is the first study that provides such formulas for various mass transfer rate coefficients for a wide range of conditions in a partially saturated soil capillary.

2. Methodology

2.1. Mathematical Model

A mathematical model, describing the transport and deposition of nanoparticles in a single partially saturated soil capillary with a length L , is presented in this section. The pore is assumed to be a parallelepiped with an angular cross-section. Figure 1a shows the triangular cross-section of a very low saturated pore, which is filled with air in middle and water in corners. The pore wall is assumed to be hydrophilic and hence, the water phase is present in

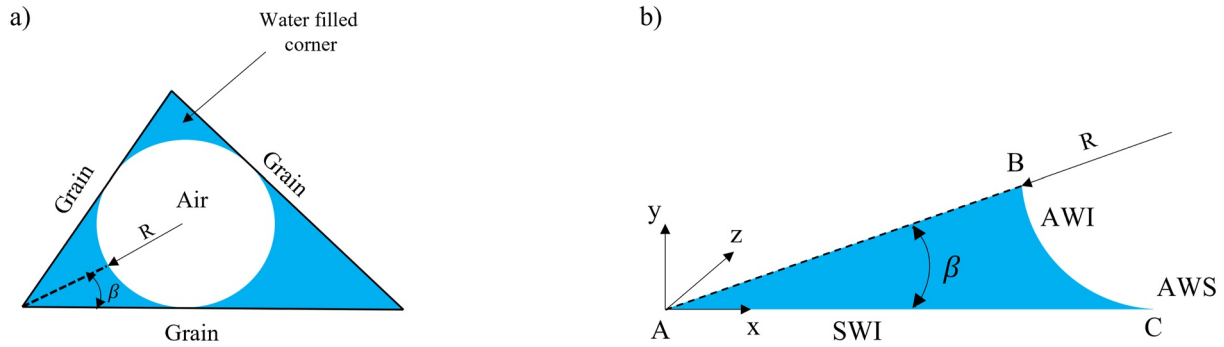


Figure 1. Conceptual representation of (a) the partially filled triangular cross-section of a soil capillary, and (b) half-corner region as the computational domain.

the pore corners only. The presence of air and water inside the pore creates two interfaces, namely SWI and AWI, and a common region, AWS line, where the three phases intersect. Due to symmetry, we consider the computational domain to be the half-corner region of water-occupied corner, as shown in Figure 1b, where, β represents the half-corner angle, and R is the radius of curvature of the AWI.

Various assumptions involved in the model are: (a) flow is fully developed, laminar, and at steady state; (b) the suspension of nanoparticles is dilute and stable, and hence, particle-particle interactions are neglected; (c) nanoparticles, AWI, and SWI are assumed to be negatively charged; (d) hydrodynamic wall effects which effect the transport of particles are neglected; and (e) particles are sufficiently small such that gravitational and lift forces are neglected.

All governing equations of flow and transport are introduced in Text S1 in Supporting Information S1 in detail. The equations have been made dimensionless, as described in Text S2 in Supporting Information S1. In this section, we provide the full set of dimensionless equations that have been solved numerically, using COMSOL Multiphysics software (version 5.6). Flow of water along the half-corner region of the pore is governed by the Stokes equation and continuity equation. Their dimensionless forms (developed in Text S2 in Supporting Information S1) are:

$$\frac{\partial^2 v_z^*}{\partial x^{*2}} + \frac{\partial^2 v_z^*}{\partial y^{*2}} = 1 \quad (1a)$$

$$\frac{\partial v_z^*}{\partial z^*} = 0 \quad (1b)$$

Here, $v_z^* [-]$ is the dimensionless flow velocity in the z direction, and x^* , y^* , and z^* are dimensionless distances along x , y , and z directions, respectively. Equations 1a and 1b are solved subject to constant pressure conditions at the inlet and the outlet of the pore with a unit dimensionless pressure gradient in the z -direction along with the following boundary conditions:

$$v_z^*(x^*, 0, z^*) = 0 \quad (2)$$

$$\left. \frac{\partial v_z^*}{\partial n^*} \right|_{AWI}(z^*) = 0 \quad (3)$$

$$\left. \frac{\partial v_z^*}{\partial n^*} \right|_{AB}(z^*) = 0 \quad (4)$$

Equation 2 represents no-slip boundary condition at the SWI, Equation 3 represents stress-free boundary condition at AWI, and Equation 4 represents symmetry condition at AB line of symmetry (see Figure 1b).

The transport of nanoparticles in the pore is modeled using the following dimensionless advection-diffusion equation:

$$\frac{\partial c^*}{\partial t^*} = \frac{1}{Pe} \left(\frac{\partial^2 c^*}{\partial x^{*2}} + \frac{\partial^2 c^*}{\partial y^{*2}} + \frac{\partial^2 c^*}{\partial z^{*2}} \right) - \frac{v_z^*}{v_m^*} \frac{\partial c^*}{\partial z^*} \quad (5)$$

where, c^* is the dimensionless nanoparticle concentration, Pe is the Peclet number, $v_z^*(x^*, y^*)$ is the dimensionless pore-water velocity, and v_m^* is the dimensionless mean pore-water velocity. For solving this equation, we need

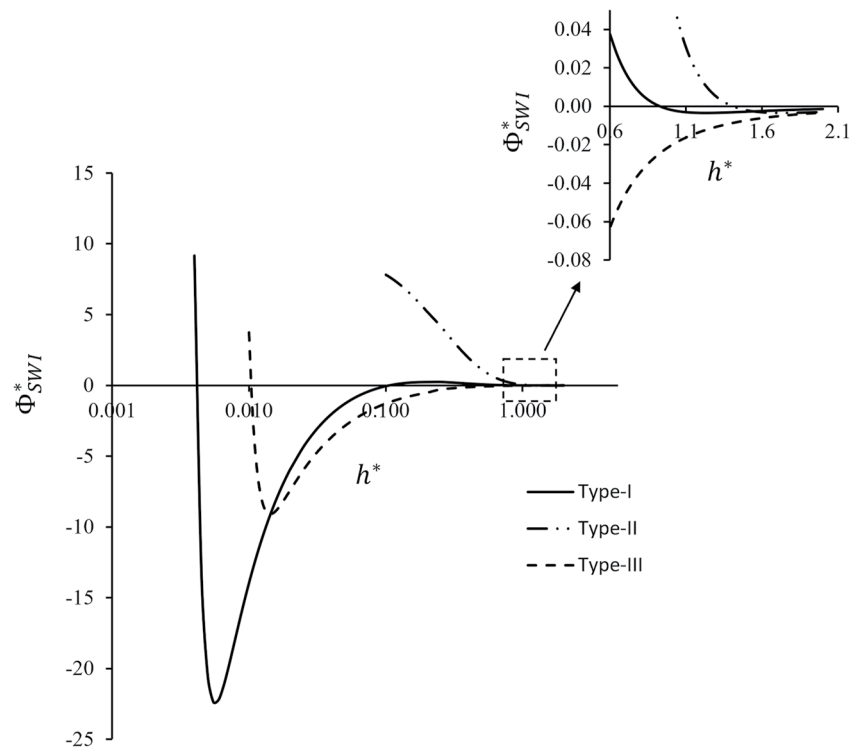


Figure 2. Types of interaction energy profiles for nanoparticles with solid-water interface (SWI). The secondary minimum region is enlarged and shown in the inset.

boundary conditions at inlet and outlet of the pore as well along SWI and AWI. Nanoparticle deposition on SWI and AWI depends on the particle-interface interaction forces which act within a distance of a few 100 nm from the interface (Elimelech et al., 1998; Lazouskaya & Jin, 2008; Ruckenstein & Prieve, 1973). Three different profiles of energy distribution (Types I, II, and III) for nanoparticle interactions with SWI and AWI are shown in Figures 2 and 3, respectively. There, Φ_{SWI}^* and Φ_{AWI}^* denote the total dimensionless interaction energies between a particle and SWI and AWI, respectively, and h^* is the dimensionless distance between the particle and the interface. There are three different regions in the energy profiles: primary minimum (in Types I and III), secondary minimum (in Types I and II), and energy barrier (in Types I and II). Types I and II energy profiles represent unfavorable conditions for deposition due to the presence of an energy barrier, whereas Type III energy profile represents a favorable condition for deposition. The calculation of interaction energies for particle-SWI and particle-AWI interactions are given in Text S3 in Supporting Information S1. The type of the energy profile between particles and SWI depends on the particle size, the surface potentials of the nanoparticle and SWI, solution ionic strength, and the Hamaker constant for particle-water-solid surface (refer to Text S3 in Supporting Information S1). For example, Type II energy profile at SWI occurs for relatively larger magnitudes of surface potentials of both nanoparticles and SWI, and smaller values of ionic strength and Hamaker constant for particle-water-solid surface. Due to its shallow depth, the secondary minimum deposited particles are reversibly attached. However, Type III energy profile occurs for relatively smaller magnitudes of surface potentials of nanoparticles and SWI, and larger values of ionic strength and Hamaker constant. The primary minimum depth of Type III profile at SWI is finite, and the particles deposited there can get detached if they can overcome the primary minimum attraction through Brownian motion. Type I energy profile has the characteristics of both Types II and III profiles, and particle deposition can happen at both secondary and primary minima. The favourability of Type I profile for deposition depends on the relative magnitudes of the primary and secondary minima depths and energy barrier height. The type of the energy profile between particles and AWI depends on the contact angle of the particles with AWI, particle size, the surface potentials of the nanoparticle and AWI, solution ionic strength, and the Hamaker constant for particle-water-AWI, with the contact angle playing the major role (refer to Text S3 in Supporting Information S1). Type II energy profile corresponds to small values of contact angle and ionic strength, relatively larger magnitudes of surface potentials of both nanoparticles and AWI, and large values of Hamaker constant.

Type III energy profile at AWI occurs for large values of the contact angle and ionic strength, relatively smaller magnitudes of surface potentials of both nanoparticles and AWI, and small values of Hamaker constant. Since the depth of the primary minimum is infinite for Types I and III energy profiles at AWI, particles deposited there are assumed to be irreversibly attached. Also, the secondary minimum deposited particles at Types I and II profiles at AWI are assumed to be reversible due to its shallow depth.

Since the length scale over which the interaction forces act is much smaller than the pore size, the effect of nanoparticle-interface interactions can be incorporated in the form of a boundary condition for the advection-diffusion equation (Equation 2) of the bulk phase (Ruckenstein & Prieve, 1973; Seetha et al., 2015; Spielman & Friedlander, 1974). The interfacial conditions at SWI and AWI are presented in Text S1 in Supporting Information S1 and made nondimensional in Text S2 in Supporting Information S1. Assuming the mass exchange between the bulk water and SWI to follow a first-order kinetics, the boundary condition at bulk-SWI in dimensionless form is

$$-\frac{1}{Pe} \frac{\partial c^*}{\partial n^*} \Big|_{SWI} = Da_{swi}^{bs} c^* \Big|_{SWI} - Da_{swi}^{sb} s_{2,swi}^* \quad \text{for Type I and Type II energy profiles at SWI} \quad (6a)$$

$$-\frac{1}{Pe} \frac{\partial c^*}{\partial n^*} \Big|_{SWI} = Da_{swi}^{bp} c^* \Big|_{SWI} - Da_{swi}^{pb} s_{1,swi}^* \quad \text{for Type III energy profile at SWI} \quad (6b)$$

Here, $s_{1,swi}^*$ [-] and $s_{2,swi}^*$ [-] are dimensionless average concentrations of particles adsorbed to SWI in the primary and secondary minima regions, respectively, Da_{swi}^{bs} and Da_{swi}^{sb} are advective Damkohler numbers corresponding for forward and backward mass transfer of particles between bulk and secondary minimum region at SWI for Types I and II profiles, respectively, and Da_{swi}^{bp} and Da_{swi}^{pb} are advective Damkohler numbers at SWI but for Type III energy profile for particle transport from bulk to primary minimum region, and primary minimum to bulk region, respectively. The calculation of advective Damkohler numbers at SWI using the interaction energy profile between particle and SWI is given in Text S1, Text S2, and Text S3 in Supporting Information S1. Similarly, assuming the mass exchange between the bulk water and AWI to follow a first-order kinetics, the boundary condition to advection-diffusion equation at AWI in dimensionless form is given as:

$$-\frac{1}{Pe} \frac{\partial c^*}{\partial n^*} \Big|_{AWI} = Da_{awi}^{bs} c^* \Big|_{AWI} - Da_{awi}^{sb} s_{2,awi}^* \quad \text{for Type I and Type II energy profiles at AWI} \quad (7a)$$

$$-\frac{1}{Pe} \frac{\partial c^*}{\partial n^*} \Big|_{AWI} = Da_{awi}^{bp} c^* \Big|_{AWI} \quad \text{for Type III energy profile at AWI} \quad (7b)$$

where, $s_{2,awi}^*$ [-] is the dimensionless average adsorbed concentration in the secondary minimum region of the energy profile at AWI, Da_{awi}^{bs} and Da_{awi}^{sb} are the advective Damkohler numbers at AWI for Types I and II profiles for particle transport from bulk to secondary minimum region, and secondary minimum to bulk region, respectively, and Da_{awi}^{bp} is the advective Damkohler number at AWI for Type III profile for particle transport from bulk to primary minimum region. The calculation of advective Damkohler numbers at AWI using the interaction energy profile between particle and AWI is given in Text S1, Text S2, and Text S3 in Supporting Information S1. The attachment to primary minimum region at AWI is assumed to be irreversible (Equation 7b) due to its infinite depth (Figure 3) and the particles there are retained by strong capillary forces.

We need to provide mass balance equations for particles that are attached to SWI, AWI, and AWS. Equations S5a and S5b (see Text S1 in Supporting Information S1), representing the governing equations for average adsorbed concentration of nanoparticles in the secondary and primary minima regions for a Type I profile at SWI, can be written in dimensionless form as given in Equations 8a and 8b, respectively.

$$\frac{\partial s_{2,swi}^*}{\partial t^*} = Da_{swi}^{bs} c^* \Big|_{SWI} - Da_{swi}^{sb} s_{2,swi}^* - Da_{swi}^{sp} s_{2,swi}^* + Da_{swi}^{ps} s_{1,swi}^* \quad (8a)$$

$$\frac{\partial s_{1,swi}^*}{\partial t^*} = Da_{swi}^{sp} s_{2,swi}^* - Da_{swi}^{ps} s_{1,swi}^* \quad (8b)$$

Here, Da_{swi}^{sp} and Da_{swi}^{ps} are the advective Damkohler numbers at SWI for Type I energy profile for particle transport from secondary to primary minimum region, and primary minimum to secondary minimum region, respectively. Note that the particles attached to SWI in the secondary minimum region may be transferred to the primary minimum region. This exchange is accounted for by the last two terms in Equation 8a. The driving force for

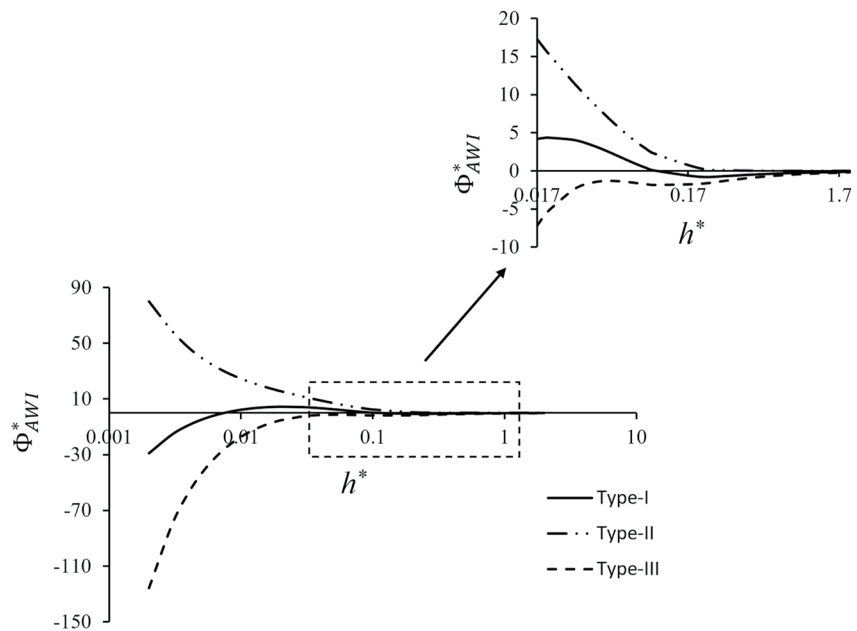


Figure 3. Types of interaction energy profiles of nanoparticles with air-water interface (AWI). The secondary minimum region is enlarged and shown in the inset.

particle transport from the primary to the secondary minimum region and vice versa is the kinetic energy of the particles due to its Brownian motion. The mass transfer rate coefficients and the corresponding advective Damkohler numbers for particle transfer from bulk to secondary minimum region, secondary minimum region to bulk, secondary minimum region to primary minimum region, and primary minimum region to secondary minimum region are all functions of both interaction energy and the particle diffusion coefficient (see Text S1 and Text S2 in Supporting Information S1). If the kinetic energy of particles imparted by Brownian motion is greater than the energy barrier to detachment from primary minimum, which is the sum of the primary minimum depth and energy barrier height, then the particles will detach from the primary minimum. This results in a large value for Da_{swi}^{ps} . Else, the value of Da_{swi}^{ps} will be small, indicating slow detachment. Similarly, if the kinetic energy of particles imparted by Brownian motion is greater than the energy barrier to attachment at primary minimum, which is the sum of the secondary minimum depth and energy barrier height, then the value of Da_{swi}^{sp} will be large and the particles will move from secondary minimum to the primary minimum. The diffusion energy is inversely proportional to particle size. Hence, for a given set of chemical conditions, the larger particles will have a lesser chance of jumping the energy barrier to attach to the primary minimum than the smaller ones.

Equations S6 and S7 (refer to Text S1 in Supporting Information S1), representing the governing equations for average adsorbed concentration of nanoparticles at SWI for Types II and III profiles, can be written in dimensionless form as given in Equations 9 and 10, respectively.

$$\frac{\partial s_{2,swi}^*}{\partial t^*} = Da_{swi}^{bs} c^* |_{SWI} - Da_{swi}^{sb} s_{2,swi}^* \quad (9)$$

$$\frac{\partial s_{1,swi}^*}{\partial t^*} = Da_{swi}^{bp} c^* |_{SWI} - Da_{swi}^{pb} s_{1,swi}^* \quad (10)$$

Particles attached to AWI are assumed to be mobile due to advection (as molecules forming AWI do not have a zero average velocity and may move along the flow direction) and diffusion within the interface (caused by Brownian motion and rotation; Lemelle et al., 2010; Stocco et al., 2019; Tan et al., 2009; Toro-Mendoza et al., 2017). Though many researchers have reported that the particle diffusion coefficient at liquid-gas interface is different from that in the bulk water due to the difference in the viscosity of the two domains (Manoharan, 2015), a quantitative relationship between the two does not exist. Hence, for simplicity, we assume that the particle diffusion coefficient within AWI to be the same as that in the bulk water. The dimensionless form of the governing

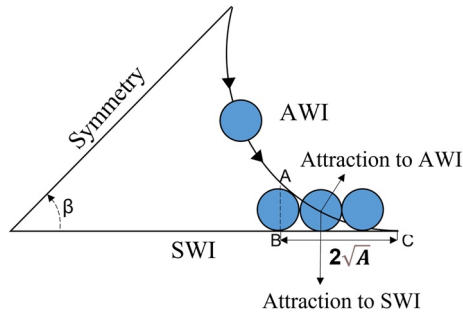


Figure 4. Schematic representation of particle transfer from air-water interface (AWI) to air-water-solid (AWS).

equations for average adsorbed concentration of nanoparticles at AWI for Type I profile (Equations S8a and S8b in Text S1 in Supporting Information S1) is given in Equations 11a and 11b, respectively.

$$\frac{\partial s_{2,awi}^*}{\partial t^*} = \frac{1}{Pe} \left[\frac{\partial^2 s_{2,awi}^*}{\partial x^{*2}} + \frac{\partial^2 s_{2,awi}^*}{\partial y^{*2}} + \frac{\partial^2 s_{2,awi}^*}{\partial z^{*2}} \right] - \frac{v_z^*|_{AWI}}{v_m^*} \frac{\partial s_{2,awi}^*}{\partial z^*} + Da_{awi}^{bs} c^*|_{AWI} - Da_{awi}^{sb} s_{2,awi}^* - Da_{awi}^{sp} s_{2,awi}^* \quad (11a)$$

$$\frac{\partial s_{1,awi}^*}{\partial t^*} = \frac{1}{Pe} \left[\frac{\partial^2 s_{1,awi}^*}{\partial x^{*2}} + \frac{\partial^2 s_{1,awi}^*}{\partial y^{*2}} + \frac{\partial^2 s_{1,awi}^*}{\partial z^{*2}} \right] - \frac{v_z^*|_{AWI}}{v_m^*} \frac{\partial s_{1,awi}^*}{\partial z^*} + Da_{awi}^{sp} s_{2,awi}^* \quad (11b)$$

Here, $s_{1,awi}^* [-]$ is the dimensionless average adsorbed concentration in the primary minimum region of the energy profile at AWI, $Da_{awi}^{sp} [-]$ is the advective Damkohler number at AWI for Type I energy profile for particle transport from secondary to primary minimum region, and $v_z^*|_{AWI}$ is the dimensionless velocity at AWI. Since the secondary minimum region is away from the AWI and particles experience a weak attractive force there, the secondary minimum deposited particles can get detached and reach the bulk fluid if the kinetic energy due to Brownian motion is larger than the attractive energy at secondary minimum. We have assumed that the average velocity of molecules forming AWI is the same as the bulk water velocity at the interface.

The governing equation for average adsorbed concentration of nanoparticles at AWI for Type II profile (Equation S9 in Text S1 in Supporting Information S1) can be written in dimensionless form as follows:

$$\frac{\partial s_{2,awi}^*}{\partial t^*} = \frac{1}{Pe} \left[\frac{\partial^2 s_{2,awi}^*}{\partial x^{*2}} + \frac{\partial^2 s_{2,awi}^*}{\partial y^{*2}} + \frac{\partial^2 s_{2,awi}^*}{\partial z^{*2}} \right] - \frac{v_z^*|_{AWI}}{v_m^*} \frac{\partial s_{2,awi}^*}{\partial z^*} + Da_{awi}^{bs} c^*|_{AWI} - Da_{awi}^{sb} s_{2,awi}^* \quad (12)$$

The governing equation for average adsorbed concentration of nanoparticles at AWI for Type III profile (Equation S10 in Text S1 in Supporting Information S1) can be written in dimensionless form as follows:

$$\frac{\partial s_{1,awi}^*}{\partial t^*} = \frac{1}{Pe} \left[\frac{\partial^2 s_{1,awi}^*}{\partial x^{*2}} + \frac{\partial^2 s_{1,awi}^*}{\partial y^{*2}} + \frac{\partial^2 s_{1,awi}^*}{\partial z^{*2}} \right] - \frac{v_z^*|_{AWI}}{v_m^*} \frac{\partial s_{1,awi}^*}{\partial z^*} + Da_{awi}^{bp} c^*|_{AWI} \quad (13)$$

Colloids at AWI have been observed to diffuse along AWI to reach AWS where they are retained irreversibly due to strong capillary forces and film straining (Butt et al., 2005, Crist et al., 2004, 2005; Gao et al., 2008; Ishida, 2007; Shang et al., 2008; Sharma et al., 2008, Zevi et al., 2005, 2012). Zevi et al. (2005) observed that polystyrene latex colloids were retained irreversibly in the contact region where the thickness of the water film was smaller than the diameter of the particle. In this study, we assume that the particles attached to AWI can move toward AWS through diffusion with the rate coefficient for particle transport from AWI to AWS to be the same as that from bulk to AWI. Figure 4 shows a schematic representation of particle retention at AWS, where the location of the vertical line AB represents the horizontal distance from the contact point, C, beyond which the water film thickness is greater than particle diameter, and hence, particles are not retained by capillary forces. Particles are retained irreversibly by film straining and capillary forces in the region ABC, where particle size is greater than or equal to the water film thickness. Particles in the region ABC are assumed to be retained irreversibly at AWS, and the line AB is taken as the boundary in numerical simulations representing AWS. The flux continuity condition at the contact line for a zero-contact angle of AWI with the solid surface in dimensionless form is given as

$$-\frac{1}{Pe} \left(\frac{\partial s_{awi}^*}{\partial x^*} + \frac{\partial s_{awi}^*}{\partial y^*} \right) \Big|_A = Da_{aws} \left(1 - \frac{s_{aws}^*}{s_{max}^*} \right) s_{awi}^*|_A \quad (14)$$

Here, $s_{awi}^* [-]$ is the dimensionless total adsorbed particle concentration at AWI, $s_{awi}^* = s_{1,awi}^* + s_{2,awi}^*$ for a Type I profile, $s_{awi}^* = s_{2,awi}^*$ for Type II energy profile, and $s_{awi}^* = s_{1,awi}^*$ for Type III energy profile, $s_{aws}^* [-]$ is the dimensionless average adsorbed concentration at AWS (number of adsorbed particles per length of contact line in dimensionless form), $Da_{aws} [-]$ is the advective Damkohler number for mass transfer from AWI to AWS, and

is assumed to be equal to (a) Da_{awi}^{bs} for Types I and II energy profiles at AWI, and (b) Da_{awi}^{bp} for Type III energy profile at AWI, and s_{max}^* [-] is the dimensionless maximum sorption capacity of AWS.

The dimensionless form of the governing equation for average adsorbed concentration of nanoparticles at AWS (Equation S12 in Text S1 in Supporting Information S1) is

$$\frac{\partial s_{aws}^*}{\partial t^*} = Da_{aws} \left(1 - \frac{s_{aws}^*}{s_{max}^*} \right) s_{awi}^* | A \quad (15)$$

In addition to the boundary conditions given in Equations 6, 7, and 14, the following initial and boundary conditions are also needed to solve the coupled set of governing equations for transport:

$$\begin{aligned} c^*(x^*, y^*, z^*, 0) = 0; \quad s_{1,swi}^*(x^*, z^*, 0) = 0; \quad s_{2,swi}^*(x^*, z^*, 0) = 0; \\ s_{1,awi}^*(x^*, y^*, z^*, 0) = s_{2,awi}^*(x^*, y^*, z^*, 0) = s_{aws}^*(z^*, 0) = 0 \end{aligned} \quad (16)$$

$$c^*(x^*, y^*, 0, t^*) = \begin{cases} 1; & t^* \leq t_{in}^* \\ 0; & t^* > t_{in}^* \end{cases} \quad (17)$$

$$s_{1,awi}^*(x^*, y^*, 0, t^*) = s_{2,awi}^*(x^*, y^*, 0, t^*) = 0 \quad (18)$$

$$\frac{\partial c^*}{\partial z^*}(x^*, y^*, L^*, t^*) = 0 \quad (19)$$

$$\left. \frac{\partial s_{1,awi}^*}{\partial z^*} \right|_{AWI}(L^*, t^*) = \left. \frac{\partial s_{2,awi}^*}{\partial z^*} \right|_{AWI}(L^*, t^*) = 0 \quad (20)$$

Here, t_{in}^* is the duration of injection of nanoparticle suspension at pore inlet.

The set of dimensionless governing Equation 5, one among 8–10 for SWI, one among 11–13 for AWI, and 15 subject to appropriate initial and boundary conditions as given in Equations 6, 7, 14, and 16–20 are solved numerically using COMSOL Multiphysics software (version 5.6). For comparison with the solution of 1D advection-dispersion-adsorption equation, we need to have the breakthrough curve at a given position. We have selected the position $z^* = 5.0$ and have averaged the 3D field of nanoparticle concentration obtained from the pore-scale model over a control volume between $z^* = 4.5$ and 5.5 and over the whole water-wetted cross-section of the half corner region of the pore. This results in obtaining the 1D-averaged dimensionless nanoparticle concentration, i.e., $\overline{c^*}|_{z^*=5.0}(t^*)$. Similarly, the 1D-averaged dimensionless concentrations adsorbed on SWI (i.e., $\overline{s_{swi}^*}$), AWI (i.e., $\overline{s_{awi}^*}$), and AWS (i.e., $\overline{s_{aws}^*}$) at $z^* = 5.0$ are obtained by averaging the corresponding adsorbed concentrations within the same control volume.

2.2. Pore-Scale Parameters

Table 1 lists the 12 dimensionless parameters involved in the pore-scale model developed in this study along with the typical range of their values, which are obtained from data reported in the literature (Crist et al., 2005; C. M. Park et al., 2016; Patzek, 2000; Patzek & Kristensen, 2001; Qi et al., 2014; Schafer, Harms, et al., 1998; Seetha et al., 2014, 2015; van Oss, 2006; Wang et al., 2017; Williams & Berg, 1992). Except for the parameter b_1 , we chose three specific values for each parameter within its range as given in Table 1. The 3D model presented above was run for a large number of random combinations of these pore-scale parameters (in total 3,601 runs). For each run, the averaged nanoparticle breakthrough concentration curve was obtained. The resulting data were fitted to the 1D advection-dispersion-adsorption equation presented below.

2.3. 1D-Averaged Model

The average transport behavior of nanoparticles in z -direction can be described using a 1D advection-dispersion equation with three-site kinetics, which account for nanoparticle deposition on SWI, AWI, and AWS. These are:

$$\frac{\partial \overline{c^*}}{\partial t^*} = \frac{1}{Pe_{(1D)}} \frac{\partial^2 \overline{c^*}}{\partial z^{*2}} - \frac{\partial \overline{c^*}}{\partial z^*} - Da_{swi}^a \overline{c^*} + Da_{swi}^d \overline{s_{swi}^*} - Da_{awi}^a \overline{c^*} + Da_{awi}^d \overline{s_{awi}^*} \quad (21)$$

Table 1
Pore-Scale Parameters Involved in the Model Developed in This Study

Parameter	Expression	Description	Range	Chosen values
λ^*	$\frac{\lambda}{a}$	Ratio of characteristic wavelength of interaction to nanoparticle radius	1–10	1, 2, and 10
β	–	Half corner angle	0.087–1.31 radians	0.087, 0.785, and 1.31
Pe	$\frac{v_m R}{D}$	Peclet number	0.05–50	0.05, 5, and 50
A	$\frac{a}{R}$	Interception parameter (ratio of nanoparticle radius to radius of curvature of AWI)	4×10^{-5} to 0.005	4×10^{-5} , 0.0001, and 0.001 ($\lambda^* = 10$) 4×10^{-5} , 0.001, and 0.005 ($\lambda^* = 1$ and 2)
b_1	–	System-specific hydrophobic constant	–21 to –22	–21 and –22
a_1	–	System-specific hydrophobic constant	–5 to –7	–5, –6, and –7
H^*	$\frac{H}{k_B T}$	Dimensionless Hamaker constant for particle-water-SWI	0.247–2.47	0.247, 1, and 2.47
H_a^*	$\frac{H_a}{k_B T}$	Dimensionless Hamaker constant for particle-water-AWI	–0.247 to –2.47	–0.247, –1, and –2.47
N_{DL}	κa	Ratio of nanoparticle radius to double layer thickness	5.5–100	5.5, 10, and 100 ($\lambda^* = 10$) 5.5, 25, and 100 ($\lambda^* = 2$) 5.5, 50, and 100 ($\lambda^* = 1$)
N_{E1}	$\frac{\pi \epsilon \epsilon_0 a (\psi_1^2 + \psi_2^2)}{k_B T}$	Represents the magnitude of surface potentials of nanoparticle and interface	10–400	1, 20, and 40 ($\lambda^* = 10$) 10, 40, and 200 ($\lambda^* = 2$) 10, 40, and 400 ($\lambda^* = 1$)
N_{E2}	$\frac{2(\psi_1/\psi_2)}{1 + (\psi_1/\psi_2)^2}$	Represents the ratio of surface potentials of nanoparticle and interface	0.8–1	0.8, 0.9, and 1
θ_c	–	Contact angle of nanoparticle with AWI	0 to $\frac{\pi}{2}$	0, $\frac{\pi}{3}$, and $\frac{\pi}{2}$ ($b_1 = -22$) 0, $\frac{\pi}{6}$, and $\frac{5\pi}{12}$ ($b_1 = -21$)

$$\frac{\partial \overline{s_{swi}^*}}{\partial t^*} = Da_{swi}^a \overline{c^*} - Da_{swi}^d \overline{s_{swi}^*} \quad (22)$$

$$\frac{\partial \overline{s_{awi}^*}}{\partial t^*} = -\frac{\overline{v_{awi}^*}}{v_m^*} \frac{\partial \overline{s_{awi}^*}}{\partial z^*} + Da_{awi}^a \overline{c^*} - Da_{awi}^d \overline{s_{awi}^*} - Da_{aws}^a \overline{s_{awi}^*} \quad (23)$$

$$\frac{\partial \overline{s_{aws}^*}}{\partial t^*} = Da_{aws}^a \overline{s_{aws}^*} \quad (24)$$

Here, $Pe_{(1D)}[-] = \frac{v_m R}{D_L}$ is the 1D Peclet number, $D_L [L^2 T^{-1}]$ is the Taylor dispersion coefficient of nanoparticles, $\overline{v_{awi}^*}$ is the dimensionless average velocity at AWI, $Da_{swi}^a [-] = \frac{k_{swi}^a R}{v_m}$ is the advective Damkohler number for particle attachment to SWI, $k_{swi}^a [T^{-1}]$ is the average rate coefficient for nanoparticle attachment to SWI, $Da_{swi}^d [-] = \frac{k_{swi}^d R}{v_m}$ is the advective Damkohler number for particle detachment from SWI, $k_{swi}^d [T^{-1}]$ is the average rate coefficient for nanoparticle detachment from SWI, $Da_{awi}^a [-] = \frac{k_{awi}^a R}{v_m}$ is the advective Damkohler number for particle attachment to AWI, $k_{awi}^a [T^{-1}]$ is the average rate coefficient for nanoparticle attachment to AWI and $Da_{awi}^d [-] = \frac{k_{awi}^d R}{v_m}$ is the advective Damkohler number for detachment from AWI, $k_{awi}^d [T^{-1}]$ is the average rate coefficient for nanoparticle detachment from AWI, $Da_{aws}^a [-] = \frac{k_{aws}^a R}{v_m}$ is the advective Damkohler number for particle attachment to AWS, and $k_{aws}^a [T^{-1}]$ is the average rate coefficient for nanoparticle attachment to AWS. Equations 21–24 are solved numerically by imposing the following initial and boundary conditions (Equations 25–27):

$$\overline{c^*}(z^*, 0) = 0; \overline{s_{swi}^*}(z^*, 0) = \overline{s_{awi}^*}(z^*, 0) = \overline{s_{aws}^*}(z^*, 0) = 0 \quad (25)$$

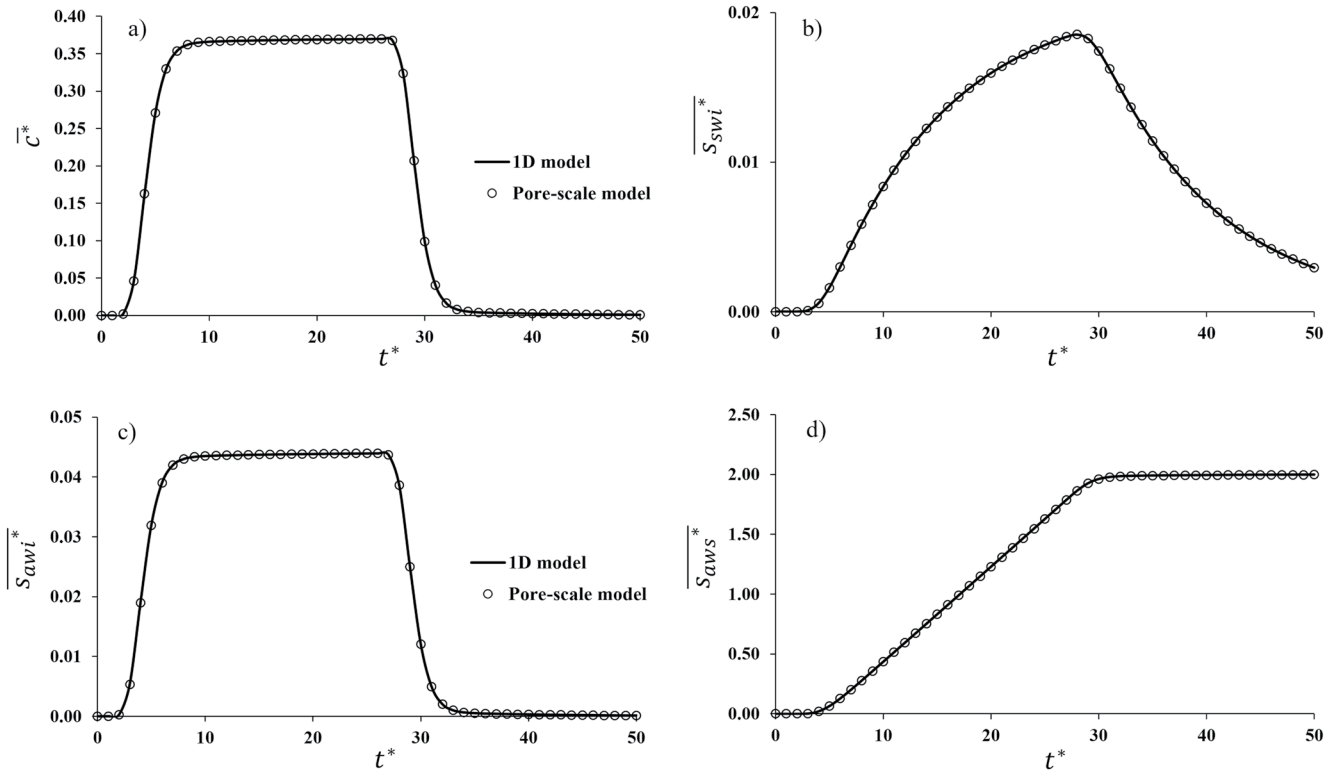


Figure 5. Comparison of (a) nanoparticle breakthrough curve, (b) adsorbed concentration curve at solid-water interface (SWI), (c) adsorbed concentration curve at air-water interface (AWI), and (d) adsorbed concentration curve at air-water-solid (AWS) obtained from the 3D pore-scale model versus the 1D averaged model. The values of parameters used in this simulation are $\lambda^* = 2$, $\beta = 45^\circ$, $Pe = 5$, $A = 0.005$, $b_1 = -21$, $a_1 = -7$, $H^* = 0.247$, $H_a^* = -0.247$, $N_{DL} = 5.5$, $N_{E1} = 10$, $N_{E2} = 1$, and $\theta_c = 0^\circ$.

$$\bar{c}^*(0, t^*) = \begin{cases} 1; & t^* \leq t_{in}^*; \\ 0; & t^* > t_{in}^* \end{cases}; \quad \overline{s_{awi}^*}(0, t^*) = 0 \quad (26)$$

$$\frac{\partial \bar{c}^*}{\partial z^*}(L^*, t^*) = 0 \quad (27)$$

The 1D-averaged model (Equations 21–24) involves six parameters ($Pe_{(1D)}$; Da_{swi}^a ; Da_{swi}^d ; Da_{awi}^a ; Da_{awi}^d ; Da_{aws}^a), whose values are estimated by following the fitting procedure as explained below. First, the value of $Pe_{(1D)}$ is estimated by simulating the transport of a conservative tracer in the pore, that is, by solving Equation 5 with zero deposition at SWI, AWI, and AWS subject to the conditions given by Equations 16, 17, and 19, and then fitting the tracer breakthrough curve (\bar{c}^* vs. t^*) with Equation 21 with $Da_{swi}^a = Da_{swi}^d = Da_{awi}^a = Da_{awi}^d = 0$. Since the particle suspension is assumed to be dilute and the particle size is between 10 and 100 nm, the adsorbed concentration of particles at SWI, AWS, and AWS will not be sufficiently large to affect the flow field, and hence, the 1D Peclet number. Hence, for simplicity, we assume in this study that nanoparticles have the same dispersivity as that of the tracer. Next, nanoparticle breakthrough curve (\bar{c}^* vs. t^*) and adsorbed concentration curves ($\overline{s_{swi}^*}$ vs. t^* , $\overline{s_{awi}^*}$ vs. t^* , and $\overline{s_{aws}^*}$ vs. t^*) obtained from the 3D pore-scale model are fitted with Equations 21–24 to estimate the values of Da_{swi}^a , Da_{swi}^d , Da_{awi}^a , Da_{awi}^d , and Da_{aws}^a . Figure 5 shows a good match between the nanoparticle breakthrough curve and adsorbed concentration curves obtained from the 3D pore-scale model and the corresponding fitted curves obtained from the 1D-averaged model. The effects of variation of each of the parameters in the 3D pore-scale model on the 1D-averaged deposition rate coefficients at SWI, AWI, and AWS, such as Da_{swi}^a , Da_{swi}^d , Da_{awi}^a , Da_{awi}^d , and Da_{aws}^a , are discussed in detail in Text S4 in Supporting Information S1.

3. Relationship Between 1D-Averaged Deposition Rate Coefficients and Pore-Scale Parameters

The 1D-averaged advective Damkohler numbers for deposition to SWI, AWI, and AWS obtained from the 3,601 simulations formed the data set that is further analyzed to find their relationship with 12 pore-scale parameters, including λ^* , β , A , Pe , b_1 , a_1 , H^* , H_a^* , N_{DL} , N_{E1} , N_{E2} , and θ_c . We found that a power-law relation could satisfactorily describe the variation of Da_{swi}^a , Da_{swi}^d , Da_{awi}^a , Da_{awi}^d , and Da_{aws}^a vis-à-vis various pore-scale parameters as given below:

$$Da_{swi}^a = k_1 \beta^{k_2} A^{-k_3} Pe^{-k_4} (2.72\lambda^*)^{-k_5} H^{*k_6} \quad (28)$$

$$Da_{swi}^d = l_1 \beta^{l_2} A^{-l_3} Pe^{-l_4} (2.72\lambda^*)^{-l_5} \quad (29)$$

$$Da_{awi}^a = m_1 \beta^{m_2} A^{m_3} Pe^{-m_4} |b_1|^{-m_5} |a_1|^{-m_6} (2.72\lambda^*)^{m_7} (\theta_c + \pi)^{m_8} \quad (30)$$

$$Da_{awi}^d = n_1 \beta^{n_2} A^{-n_3} Pe^{-n_4} |b_1|^{-n_5} |a_1|^{-n_6} (2.72\lambda^*)^{-n_7} (\theta_c + \pi)^{-n_8} \quad (31)$$

$$Da_{aws}^a = o_1 \beta^{o_2} A^{-o_3} Pe^{-o_4} |b_1|^{-o_5} |a_1|^{-o_6} (2.72\lambda^*)^{-o_7} (\theta_c + \pi)^{o_8} \quad (32)$$

Here, k_i , l_j , m_k , n_k and o_k ($i = 1, 2, \dots, 6$; $j = 1, 2, \dots, 5$; and $k = 1, 2, \dots, 8$) are the coefficients whose values are estimated through multiple-linear regression analysis. The deposition rate coefficients at SWI, Da_{swi}^a , and Da_{swi}^d , are found to be insensitive to variation in the values of parameters such as H_a^* , N_{DL} , N_{E1} , N_{E2} , b_1 , a_1 , and θ_c (refer to Text S4 and Figures S4–S6 in Supporting Information S1), and hence, are not included in Equations 28 and 29. Similarly, the deposition rate coefficients at AWI and AWS, such as Da_{awi}^a , Da_{awi}^d , and Da_{aws}^a , are found to be insensitive to parameters such as H_a^* , N_{DL} , N_{E1} , N_{E2} , and H^* (refer to Text S4 and Figure S3 in Supporting Information S1), and thus are not included in Equations 30–32. Table 2 lists the estimated values of coefficients in Equations 28–32. Figure 6 compares the predicted values of Da_{swi}^a , Da_{swi}^d , Da_{awi}^a , Da_{awi}^d , and Da_{aws}^a obtained from Equations 28–32 versus the corresponding values estimated by fitting the 3D pore-scale simulations using the 1D-averaged model. It is clear that there is a good agreement between the predicted and estimated values of Da_{swi}^a , Da_{swi}^d , Da_{awi}^a , Da_{awi}^d , and Da_{aws}^a (Figure 6). It can be inferred from Equations 28–32 that the parameters describing pore geometry (β , A , and λ^*), flow (Pe), and the hydrophobic energy (b_1 , a_1 , and θ_c) govern the retention of nanoparticles at SWI, AWI, and AWS, with negligible contribution from the chemical parameters (H_a^* , N_{DL} , N_{E1} , and N_{E2}).

Equations 28–32 are further converted into the dimensional form which results in the following relationship between 1D-averaged deposition rate coefficients at SWI, AWI, and AWS vis-à-vis various dimensional pore-scale parameters.

$$k_{swi}^a = p_1 \beta^{p_2} a^{-p_3} R^{-p_4} v_m^{p_5} H^{p_6} \mu^{-p_7} T^{p_8} \quad (33)$$

$$k_{swi}^d = q_1 \beta^{q_2} a^{-q_3} R^{-q_4} v_m^{q_5} \mu^{-q_6} T^{q_7} \quad (34)$$

$$k_{awi}^a = r_1 \beta^{r_2} a^{-r_3} R^{-r_4} |b_1|^{-r_5} |a_1|^{-r_6} v_m^{r_7} \mu^{-r_8} T^{r_9} (\theta_c + \pi)^{r_{10}} \quad (35)$$

$$k_{awi}^d = s_1 \beta^{s_2} a^{-s_3} R^{-s_4} |b_1|^{s_5} |a_1|^{-s_6} v_m^{s_7} \mu^{-s_8} T^{s_9} (\theta_c + \pi)^{-s_{10}} \quad (36)$$

$$k_{aws}^a = t_1 \beta^{t_2} a^{-t_3} R^{-t_4} |b_1|^{-t_5} |a_1|^{-t_6} v_m^{t_7} \mu^{-t_8} T^{t_9} (\theta_c + \pi)^{t_{10}} \quad (37)$$

Here, p_i , q_j , r_k , s_k and t_k ($i = 1, 2, \dots, 8$; $j = 1, 2, \dots, 7$; and $k = 1, 2, \dots, 10$) are the coefficients whose values are given in Table 2. p_1 , q_1 , r_1 , s_1 , and t_1 are calculated using the following expressions:

$$p_1 = k_1 (2.72\lambda)^{-k_5} (6\pi)^{-k_4} k_B^{(k_6 - k_4)} \quad (38)$$

$$q_1 = l_1 (2.72\lambda)^{-l_5} (6\pi)^{-l_4} k_B^{l_4} \quad (39)$$

$$r_1 = m_1 (2.72\lambda)^{m_7} (6\pi)^{-m_4} k_B^{m_4} \quad (40)$$

$$s_1 = n_1 (2.72\lambda)^{-n_7} (6\pi)^{-n_4} k_B^{n_4} \quad (41)$$

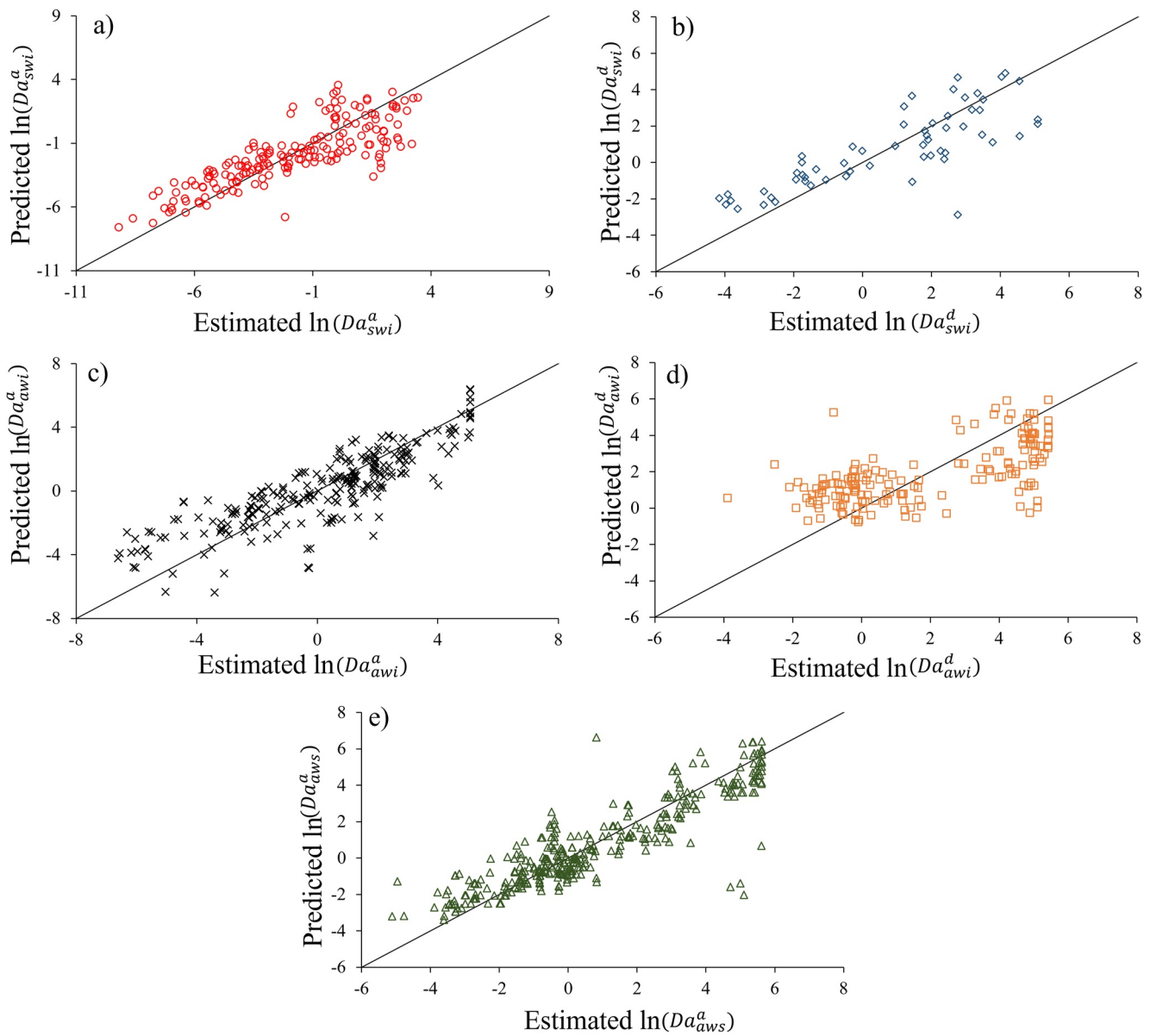


Figure 6. Comparison of predicted values of (a) Da_{swi}^a , (b) Da_{swi}^d , (c) Da_{awi}^a , (d) Da_{awi}^d , and (e) Da_{aws}^a obtained from Equations 28–32 versus the corresponding values estimated by fitting the 3D simulations with the 1D-averaged model. Straight line in all the above figures represents 1:1 line.

$$t_1 = o_1(2.72\lambda)^{-0.7}(6\pi)^{-0.4}k_B^{0.4} \quad (42)$$

Equations 35 and 36 and Table 2 show an increasing trend for k_{awi}^a and k_{awi}^d versus β . This is because an increase in the value of β leads to a decrease in the velocity of flow near the AWI. This results in increased transport of particles through diffusion toward AWI. Larger particle concentration at AWI leads to greater particle transport from AWI to AWS. Hence, k_{aws}^a shows a positive trend with increasing β (Equation 37). As the diffusion length for particles to reach SWI decreases with increasing β , k_{awi}^a shows an increasing trend with β (Equation 33 and Table 2).

Equations 33–37 and Table 2 indicate a decreasing trend for the deposition rate coefficients at SWI, AWI, and AWS versus particle size. This is due to decreasing value of particle diffusion coefficient with increasing particle size, which decreases the rate of transport of particles toward interfaces. Also, particle size plays a role in the interaction energy profiles between the particle and interface. This is also due to the decrease in depth of secondary energy minimum and increasing height of energy barrier for deposition to primary minimum for particle-AWI

with increasing particle size, which makes the conditions unfavorable for deposition. In addition, the energy barrier for deposition at SWI increases with increasing particle size.

The deposition rate coefficients of nanoparticles at SWI, AWI, and AWS decrease with increasing radius of curvature of the AWI (or increasing degree of saturation) due to larger diffusion length of particles from bulk to the interfaces (Equations 33–37 and Table 2). This is comparable to the experimental results reported in the literature which observed larger number of particles getting attached to SWI and AWI with decreasing water content of the soil (Gargiulo et al., 2008; Torkzaban et al., 2008; Wan et al., 1994; Wan & Wilson, 1994).

The rate coefficients for particle attachment to SWI, AWI and AWS increase with increasing pore-water velocity (Equations 33, 35, and 37 and Table 2). AWS offers a favorable site for particle deposition. Hence, the larger the pore-water velocity, the faster will be the rate at which particles are brought to AWI, which in turn results in greater attachment to AWS. Equations 34 and 36 show that the detachment rate coefficients of nanoparticles from SWI and AWI increase with increasing pore-water velocity. We could not find any paper in the literature where the rate coefficients of attachment/detachment of particles from/to various interfaces are reported for different pore-water velocities at the same saturation. However, the findings from this study are consistent with the studies of Gargiulo et al. (2008), Torkzaban et al. (2006), and Zhang et al. (2013, 2014) who reported increased values of attachment and detachment rate coefficients of bacteria, bacteriophages, polystyrene microspheres, and silica microspheres at SWI with increasing pore-water velocity caused by decreasing saturation (i.e., the above papers maintained a constant flow rate for different saturations). Similarly, Torkzaban et al. (2006) found increasing values of attachment and detachment rate coefficients of bacteriophages at SWI with increasing pore-water velocity caused by decreasing saturation.

Equations 35 and 37 predict greater retention of hydrophobic nanoparticles than hydrophilic ones at AWI and AWS, with k_{awi}^a and k_{aws}^a showing a positive trend with θ_c and k_{awi}^d showing a negative trend with θ_c . This is due to the greater depth of primary minimum and smaller height of energy barrier with increasing θ_c , which makes the conditions more favorable for deposition. This is in line with the results of Bradford et al. (2013) who observed greater affinity of hydrophobic colloids ($\theta_c = 65^\circ$) to AWI than relatively hydrophilic colloids ($\theta_c = 30^\circ$). Similar observations were reported by Wan and Wilson (1994), and Lazouskaya and Jin (2008). Later, Zhang et al. (2014) observed greater remobilization of hydrophilic colloids than hydrophobic colloids during imbibition as the hydrophobic particles were observed to be irreversibly attached to liquid-liquid interface and triple contact line.

4. Summary and Conclusions

A 3D mathematical model is developed to simulate the transport of nanoparticles in a water-filled corner of a partially saturated soil capillary by accounting for particle deposition at SWI, AWI, and AWS. Particle deposition rates at SWI and AWI depend on their interaction energy profiles at the interfaces. The model includes a novel formulation for particle transport from AWI interface to AWS common region, where it gets retained irreversibly by capillary forces. The contribution of AWS toward particle retention is found to increase with increasing hydrophobicity of the particles, with the SWI playing a major role in the retention of relatively hydrophilic particles. The 1D-averaged breakthrough curves and adsorbed concentration curves obtained from the 3D model are then fitted with 1D advection-dispersion-sorption equation with three-site kinetics to estimate the values of 1D-averaged deposition rate coefficients at SWI, AWI, and AWS. The geometrical parameters such as half corner angle, particle size, and radius of curvature of AWI, and mean flow velocity have been found to significantly affect the 1D-averaged deposition rate coefficients at SWI, AWI, and AWS. Moreover, the parameters representing hydrophobic energy of particles at AWI, including the contact angle of particles at AWI and hydrophobic constants, are found to have a significant effect only on 1D-averaged deposition rate coefficients at AWI and AWS, and negligible effect on particle deposition at SWI. Hamaker constant is found to have a significant effect only on particle deposition at SWI. However, chemical parameters such as surface potentials of particles, SWI, and AWI, and solution ionic strength are found to have negligible effect on 1D-averaged deposition rate coefficients at SWI, AWI, and AWS. The 1D model results are further used to develop relationships between 1D-averaged deposition rate coefficients at SWI, AWI, and AWS vis-à-vis various pore-scale parameters including half corner angle, particle size, radius of curvature of AWI, mean flow velocity, contact angle of particles with AWI, hydrophobic constants, and Hamaker constant. We found that a power-law relation describes the variation of 1D-averaged deposition rate coefficients at SWI, AWI, and AWS vis-à-vis various pore-scale parameters. The rate coefficients for particle attachment to SWI, AWI, and AWS, and detachment from SWI and AWI increase with increasing half corner angle, and mean flow velocity, and decrease with increasing radius of curvature of AWI and particle radius. In addition, the rate coefficient for particle attachment to SWI increases with increasing

Hamaker constant, and the rate coefficients for particle attachment to AWI and AWS increase with increasing contact angle of particle with AWI. Moreover, the rate coefficient for particle detachment from AWI decreases with increasing contact angle of particle with AWI.

We assumed in this study that the diffusion coefficients of nanoparticles in bulk and at AWI to be the same. However, this assumption is not always true. The diffusive force experienced by a particle at AWI depends on the amount of protrusion of the particle at AWI, which in turn depends on the difference in the viscosities of air and water. Since water is more viscous than air, particles will protrude more toward the air and thus will have lesser contact area with water phase. Boniello et al. (2015) found that the viscous drag force acting on particles increased with decreasing contact area of particles with the water, and hence, the translational diffusion coefficient decreased. Radoev et al. (1992) estimated the diffusion coefficient of particles of size between 0.5 and 0.9 μm in the bulk and AWI to be 0.6 and 0.4 $\mu\text{m}^2/\text{s}$, respectively. Hence, if the nanoparticle diffusion coefficient at AWI is smaller than that in the bulk, then the mass transfer rate coefficient for particle transfer from secondary minimum at AWI (Types I and II energy profiles) to bulk decreases and also, the transfer rate from AWI to AWS decreases. As a result, the average rate coefficients for nanoparticle detachment from AWI (k_{awi}^d) and attachment to AWS (k_{aws}^a) will be smaller than the values estimated in this study.

This is the first study where nanoparticle transport is simulated in a single partially saturated pore under a wide range of physicochemical conditions. We have obtained relationships for 1D-averaged deposition rate coefficients at SWI, AWI, and AWS vis-à-vis various physicochemical parameters. These relationships can be further incorporated into a pore-network model to upscale nanoparticle transport to the continuum scale. Of course, a pore network model may involve both fully saturated and partially saturated pores. The formulations for 1D-averaged deposition rate coefficients at SWI, AWI, and AWS proposed in this study are applicable only for partially drained pores. For fully saturated pores, the deposition rate coefficients at SWI can be calculated using the formulations proposed by Seetha et al. (2017), or by following the approach of Lin et al. (2021, 2022).

Notation

a	nanoparticle radius [L]
a_1	system-specific hydrophobic constant [-]
A	interception parameter [-]
b_1	system-specific hydrophobic constant [-]
c	nanoparticle number concentration in the pore [no. L^{-3}]
c^*	dimensionless nanoparticle concentration [-]
$\overline{c^*}$	dimensionless nanoparticle breakthrough concentration [-]
c_0	nanoparticle concentration at the pore inlet [no. L^{-3}]
D	particle diffusion coefficient [$\text{L}^2 \text{T}^{-1}$]
D_L	nanoparticle dispersion coefficient
Da_{awi}^a	advective Damkohler number for particle attachment to AWI [-]
Da_{awi}^{bp}	advective Damkohler number at AWI for particle transport from bulk to primary minimum region [-]
Da_{awi}^{bs}	advective Damkohler number at AWI for particle transport from bulk to secondary minimum region [-]
Da_{awi}^d	advective Damkohler number for detachment from AWI [-]
Da_{awi}^{sb}	advective Damkohler number at AWI for particle transport from secondary minimum to bulk region [-]
Da_{awi}^{sp}	advective Damkohler number at AWI for particle transport from secondary to primary minimum region [-]
Da_{aws}^a	advective Damkohler number for particle attachment to AWS [-]
Da_{swi}^a	advective Damkohler number for particle attachment to SWI [-]
Da_{swi}^{bp}	advective Damkohler number corresponding for mass transfer of particles between bulk and primary minimum region at SWI
Da_{swi}^{bs}	advective Damkohler number corresponding for mass transfer of particles between bulk and secondary minimum region at SWI [-]

Da_{swi}^d	advective Damkohler number for particle detachment from SWI [-]
Da_{swi}^{pb}	advective Damkohler number corresponding for mass transfer of particles between primary minimum and bulk region at SWI [-]
Da_{swi}^{ps}	advective Damkohler numbers at SWI for particle transport from primary minimum to secondary minimum region [-]
Da_{swi}^{sb}	advective Damkohler number corresponding for mass transfer of particles between secondary minimum and bulk region at SWI [-]
Da_{swi}^{sp}	advective Damkohler number at SWI for particle transport from secondary to primary minimum region [-]
Da_{aws}	advective Damkohler number for mass transfer from AWI to AWS
e	elementary charge [-]
h	separation distance between the particle surface and the interface [L]
h^*	dimensionless distance between the particle and the interface [-]
H^*	dimensionless Hamaker constant for SWI [-]
H_a^*	dimensionless Hamaker constant for AWI [-]
I	solution ionic strength [Molar]
k_{132}	force constant for asymmetric interactions between nanoparticles and AWI in water [$M L^2 T^{-2}$]
k_B	Boltzmann constant [$M^1 L^2 T^{-2} K^{-1}$]
k_{awi}^a	average rate coefficient for nanoparticle attachment to AWI [T^{-1}]
k_{awi}^{bp}	rate coefficient mass transfer of particles between bulk and primary minimum region at AWI [$L T^{-1}$]
$k_{awi}^{bs}, k_{awi}^{sb}$	rate coefficients for forward [$L T^{-1}$] and backward [T^{-1}] mass transfer of particles between bulk and secondary minimum region at AWI respectively
k_{awi}^d	average rate coefficient for nanoparticle detachment from AWI [T^{-1}]
k_{awi}^{sp}	mass transfer rate coefficient at AWI for particle transport from secondary to primary minimum region [T^{-1}]
k_{aws}	mass transfer rate coefficient from AWI to AWS [$L T^{-1}$]
k_{aws}^a	average rate coefficient for nanoparticle attachment to AWS [T^{-1}]
k_{swi}^a	average rate coefficient for nanoparticle attachment to SWI [T^{-1}]
$k_{swi}^{bp}, k_{swi}^{pb}$	rate coefficients for forward [$L T^{-1}$] and backward [T^{-1}] mass transfer of particles between bulk and primary minimum region at SWI respectively
$k_{swi}^{bs}, k_{swi}^{sb}$	rate coefficients for forward [$L T^{-1}$] and backward [T^{-1}] mass transfer of particles between bulk and secondary minimum region at SWI respectively
k_{swi}^d	average rate coefficient for nanoparticle detachment from SWI [T^{-1}]
$k_{swi}^{sp}, k_{swi}^{ps}$	mass transfer rate coefficients at SWI for particle transport from secondary to primary minimum region, and primary minimum to secondary minimum region, respectively [T^{-1}]
N_A	Avogadro's number
N_{DL}	dimensionless parameter representing the ratio of nanoparticle radius to double layer thickness [-]
N_{E1}	dimensionless parameter representing the magnitudes of surface potentials [-]
N_{E2}	dimensionless parameter representing the ratio of surface potentials [-]
p	fluid pressure [$M^1 L^{-1} T^{-2}$]
Pe	Peclet number [-]
$Pe_{(1D)}$	1D Peclet number [-]
R	radius of curvature of the AWI [L]
$s_{1,awi}, s_{2,awi}$	average concentrations of particles adsorbed to SWI in the primary and secondary minima regions [$no L^{-2}$]
$s_{1,awi}^*$	dimensionless average adsorbed concentration in the primary minimum region of the energy profile at AWI [-]
$s_{1,swi}, s_{2,swi}$	average concentrations of particles adsorbed to SWI in the primary and secondary minima regions [$no L^{-2}$]
$s_{1,swi}^*$	dimensionless average concentration of particles adsorbed to SWI in the primary minima region [-]
$s_{2,swi}^*$	dimensionless average adsorbed concentration in the secondary minimum region of the energy profile at AWI [-]

$s_{2,swi}^*$	dimensionless average concentration of particles adsorbed to SWI in the secondary minima region [-]
s_{awi}	total adsorbed particle concentration at AWI [no L ⁻²]
s_{awi}^*	dimensionless total adsorbed particle concentration at AWI [-]
s_{aws}	average adsorbed concentration at AWS [no. L ⁻¹]
s_{aws}^*	dimensionless total adsorbed particle concentration at AWS [-]
s_{max}	maximum sorption capacity of AWS [no. L ⁻¹]
s_{max}^*	dimensionless maximum sorption capacity of AWS [-]
$\frac{s_{awi}^*}{s_{aws}^*}$	dimensionless average adsorbed concentration at AWI [-]
$\frac{s_{aws}^*}{s_{aws}^*}$	dimensionless average adsorbed concentration at AWS [-]
$\frac{s_{swi}^*}{s_{swi}^*}$	dimensionless average adsorbed concentration at SWI [-]
t	time [T]
T	absolute temperature [K]
u_m	mean pore-water velocity [L T ⁻¹]
u_m^*	dimensionless mean pore-water velocity [-]
u_z	flow velocity in the z direction [L T ⁻¹].
u_z^*	dimensionless flow velocity in the z direction
$\frac{u_{awi}^*}{u_{awi}^*}$	dimensionless average velocity at AWI [-]
$x^*, y^*, \text{ and } z^*$	dimensionless distances along x, y, and z directions, respectively
β	half corner angle
δ_{p1}	distance of the beginning of the primary minimum well from the solid surface at which $\Phi_{SWI} = 0$ [L]
δ_{p2}	location of the ending of the primary minimum well from the solid surface at which $\Phi_{SWI} = 0$ [L]
δ_s	distance from the solid surface at which $\Phi_{SWI} = 0$ in the secondary minimum region of SWI [L]
δ_ϕ	position of the SWI between the bulk and potential regions measured from the surface of the pore [L]
δ_p'	location of the ending of the primary minimum well from the solid surface at which $\Phi_{AWI} = 0$ [L]
δ_s'	distance from the solid surface at which $\Phi_{AWI} = 0$ in the secondary minimum region of AWI [L]
δ_ϕ'	position of the AWI between the bulk and potential regions measured from the surface of the pore [L]
ϵ	dielectric constant of water [-]
ϵ_0	permittivity of vacuum [M ⁻¹ L ⁻³ T ⁴ I ²]
θ_a	contact angle of AWI with SWI
θ_c	contact angle of AWI with SWI
κ	inverse Debye-Huckel length [L ⁻¹]
λ	characteristic wavelength of the interaction [L]
λ^*	dimensionless parameter representing the ratio of characteristic wavelength of the interaction to nanoparticle radius [-]
μ	dynamic viscosity of water [M L ⁻¹ T ⁻¹]
ν	Poisson ratio [-]
σ	collision diameter [L]
σ^*	dimensionless parameter representing the ratio of collision diameter to nanoparticle radius
Φ_{Born}^s	Born potential energy between particle and solid surface [ML ² T ⁻²]
Φ_{AWI}^*	dimensionless interaction energy between nanoparticle and AWI [-]
Φ_{SWI}^*	dimensionless interaction energy between nanoparticle and SWI [-]
Φ_{EDL}^s	electric double layer energy between particle and solid surface [M L ² T ⁻²]
Φ_{EDL}^a	electrostatic double layer energy between particle and AWI [M L ² T ⁻²]
Φ_{HYD}^a	hydrophobic energy between particle and AWI [M L ² T ⁻²]
Φ_{AWI}	interaction energy between nanoparticle and AWI [M L ² T ⁻²]
Φ_{SWI}	interaction energy between nanoparticle and SWI [M L ² T ⁻²]
Φ_{vdW}^a	London van der Waals energy between particle and AWI [M L ² T ⁻²]
Φ_{vdW}^s	London van der Waals energy between particle and solid surface [M L ² T ⁻²]
ψ_1, ψ_2	surface potentials of nanoparticle and interface, respectively [ML ² I ⁻¹ T ⁻³]

Data Availability Statement

The data generated in this paper are available in the website <https://doi.org/10.6084/m9.figshare.21835674.v1>.

Acknowledgments

NS thankfully acknowledges the funding received from Department of Science and Technology, Government of India through INSPIRE Faculty Award (Sanction no. DST/INSPIRE/04/2016/000013) for carrying out this work. Moreover, SMH wishes to thank the German Research Foundation (DFG) for supporting this work through EXC2075- 390740016 under Germany's Excellence Strategy and acknowledge the support by the Stuttgart Center for Simulation Science (SimTech). The authors also acknowledge Science and Engineering Research Board (SERB), Government of India for funding SMH's visit to IIT Hyderabad through VAJRA Faculty Scheme (Sanction no. VJR/2020/000006).

References

- Abdel-Fattah, A. I., & El-Genk, M. S. (1998a). On colloidal particle sorption onto a stagnant air-water interface. *Advances in Colloid and Interface Science*, 78(3), 237–266. [https://doi.org/10.1016/s0001-8686\(98\)00066-9](https://doi.org/10.1016/s0001-8686(98)00066-9)
- Abdel-Fattah, A. I., & El-Genk, M. S. (1998b). Sorption of hydrophobic, negatively charged microsphere onto a stagnant air/water interface. *Journal of Colloid and Interface Science*, 202(2), 417–429. <https://doi.org/10.1006/jcis.1998.5442>
- Bai, R., & Tien, C. (1999). Particle deposition under unfavourable surface interactions. *Journal of Colloid and Interface Science*, 218(2), 488–499. <https://doi.org/10.1006/jcis.1999.6424>
- Boniello, G., Blanc, C., Fedorenko, D., Medfai, M., Mbarek, N. B., Gross, M., et al. (2015). Brownian diffusion of a partially wetted colloid. *Nature Materials*, 14(9), 908–911. <https://doi.org/10.1038/nmat4348>
- Bradford, S. A., & Bettahar, M. (2005). Straining, attachment, and detachment of *Cryptosporidium* oocysts in saturated porous media. *Journal of Environmental Quality*, 34(2), 469–478. <https://doi.org/10.2134/jeq2005.0469>
- Bradford, S. A., & Saeed, T. (2008). Colloid transport and retention in unsaturated porous media: A review of interface-, collector-, and pore-scale processes and models. *Vadose Zone Journal*, 7(2), 667–681. <https://doi.org/10.2136/vzj2007.0092>
- Bradford, S. A., Torkzaban, S., & Shapiro, A. (2013). A theoretical analysis of colloid attachment and straining in chemically heterogeneous porous media. *Langmuir*, 29(23), 6944–6952. <https://doi.org/10.1021/la4011357>
- Bridge, J. W., Banwart, S. A., & Heathwaite, A. L. (2007). High-resolution measurement of pore saturation and colloid removal efficiency in quartz sand using fluorescence imaging. *Environmental Science & Technology*, 41(24), 8288–8294. <https://doi.org/10.1021/es071155a>
- Butt, H.-J. (1994). A technique for measuring the force between a colloidal particle in water and a bubble. *Journal of Colloid and Interface Science*, 166(1), 109–117. <https://doi.org/10.1006/jcis.1994.1277>
- Butt, H.-J., Cappella, B., & Kappel, M. (2005). Force measurements with the atomic force microscope: Technique, interpretation and applications. *Surface Science Reports*, 59(1–6), 1–152. <https://doi.org/10.1016/j.surfrep.2005.08.003>
- Chaúque, E. F. C., Zvimba, J. N., Ngila, J. C., & Musee, N. (2014). Stability studies of commercial ZnO engineered nanoparticles in domestic wastewater. *Physics and Chemistry of the Earth, Parts A/B/C*, 67, 140–144. <https://doi.org/10.1016/j.pce.2013.09.011>
- Chen, G., & Flury, M. (2005). Retention of mineral colloids in unsaturated porous media as related to their surface properties. *Colloids and Surfaces A: Physicochemical and Engineering Aspects*, 256(2–3), 207–216. <https://doi.org/10.1016/j.colsurfa.2005.01.021>
- Chen, G., Flury, M., Harsh, J. B., & Lichtner, P. C. (2005). Colloid-facilitated transport of cesium in variably saturated Hanford sediments. *Environmental Science & Technology*, 39(10), 3435–3442. <https://doi.org/10.1021/es048978+>
- Chen, L., Sabatini, D. A., & Kibbey, T. C. G. (2008). Role of the air-water interface in the retention of TiO₂ nanoparticles in porous media during primary drainage. *Environmental Science & Technology*, 42(6), 1916–1921. <https://doi.org/10.1021/es071410r>
- Chen, L., Sabatini, D. A., & Kibbey, T. C. G. (2010). Retention and release of TiO₂ nanoparticles in unsaturated porous media during dynamic saturation change. *Journal of Contaminant Hydrology*, 118(3–4), 199–207. <https://doi.org/10.1016/j.jconhyd.2010.07.010>
- Chen, L., Sabatini, D. A., & Kibbey, T. C. G. (2012). Transport and retention of fullerene (nC60) nanoparticles in unsaturated porous media: Effects of solution chemistry and solid phase coating. *Journal of Contaminant Hydrology*, 138(139), 104–112. <https://doi.org/10.1016/j.jconhyd.2012.06.009>
- Cherrey, K. D., Flury, M., & Harsh, J. B. (2003). Nitrate and colloid transport through coarse Hanford sediments under steady state, variably saturated flow. *Water Resources Research*, 39(6), 1165. <https://doi.org/10.1029/2002WR001944>
- Choi, H., & Corapcioglu, M. Y. (1997). Transport of a non-volatile contaminant in unsaturated porous media in the presence of colloids. *Journal of Contaminant Hydrology*, 25(3–4), 299–324. [https://doi.org/10.1016/s0169-7722\(96\)00040-x](https://doi.org/10.1016/s0169-7722(96)00040-x)
- Crist, J. T., McCarthy, J. F., Zevi, Y., Baveye, P., Throop, J. A., & Steenhuis, T. S. (2004). Pore-scale visualization of colloid transport and retention in partly saturated porous media. *Vadose Zone Journal*, 3(2), 444–450. <https://doi.org/10.2136/vzj2004.0444>
- Crist, J. T., Zevi, Y., McCarthy, J. F., Throop, J. A., & Steenhuis, T. S. (2005). Transport and retention mechanisms of colloids in partially saturated porous media. *Vadose Zone Journal*, 4(1), 184–195. <https://doi.org/10.2113/4.1.184>
- Ducker, W. A., Xu, Z., & Israelachvili, J. N. (1994). Measurements of hydrophobic and DLVO forces in bubble-surface interactions in aqueous solutions. *Langmuir*, 10(9), 3279–3289. <https://doi.org/10.1021/la00021a061>
- El-Farhan, Y. H., Denovio, N. M., Herman, J. S., & Hornberger, G. M. (2000). Mobilization and transport of soil particles during infiltration experiments in an agricultural field, Shenandoah valley, Virginia. *Environmental Science & Technology*, 34(17), 3555–3559. <https://doi.org/10.1021/es991099g>
- Elimelech, M., Gregory, J., Jia, X., & Williams, R. A. (1998). *Particle deposition and aggregation measurement, modeling, and simulation*. Butterworth-Heinemann.
- Fielden, M. L., Hayes, R. A., & Ralston, J. (1996). Surface and capillary forces affecting air bubble-particle interactions in aqueous electrolyte. *Langmuir*, 12(15), 3721–3727. <https://doi.org/10.1021/la960145c>
- Flury, M., & Aramrak, S. (2017). Role of air-water interfaces in colloid transport in porous media: A review. *Water Resources Research*, 53(7), 5247–5275. <https://doi.org/10.1002/2017wr020597>
- Foppen, J. W. A., Mporokoso, A., & Schijven, J. F. (2005). Determining straining of *Escherichia coli* from breakthrough curves. *Journal of Contaminant Hydrology*, 76(3–4), 191–210. <https://doi.org/10.1016/j.jconhyd.2004.08.005>
- Gao, B., Saiers, J. E., & Ryan, J. N. (2004). Deposition and mobilization of clay colloids in unsaturated porous media. *Water Resources Research*, 40(8), W08602. <https://doi.org/10.1029/2004WR003189>
- Gao, B., Steenhuis, T. S., Zevi, Y., Morales, V. L., Nieber, J. L., Richards, B. K., et al. (2008). Capillary retention of colloids in unsaturated porous media. *Water Resources Research*, 44(4), W04504. <https://doi.org/10.1029/2006WR005332>
- Gargiulo, G., Bradford, S. S., Simunek, J., Ustohal, P., Ustohal, P., Vereecken, H., & Klumpp, E. (2008). Bacteria transport and deposition under unsaturated flow conditions: The role of water content and bacteria surface hydrophobicity. *Vadose Zone Journal*, 7(2), 406–419. <https://doi.org/10.2136/vzj2007.0068>
- Gehring, T., & Fischer, T. M. (2011). Diffusion of nanoparticles at an air/water interface is not invariant under a reversal of the particle charge. *Journal of Physical Chemistry C*, 115(48), 23677–23681. <https://doi.org/10.1021/jp2061738>

- Gomez-Suarez, C., Noordmans, J., van der Mei, H. C., & Busscher, H. J. (1999a). Detachment of colloidal particles from collector surfaces with different electrostatic charge and hydrophobicity by attachment to air bubbles in a parallel plate flow chamber. *Physical Chemistry Chemical Physics*, 1(18), 4423–4427. <https://doi.org/10.1039/a905156b>
- Gomez-Suarez, C., Noordmans, J., van der Mei, H. C., & Busscher, H. J. (1999b). Removal of colloidal particles from quartz collector surfaces as stimulated by the passage of liquid-air interfaces. *Langmuir*, 15, 5123–5127. <https://doi.org/10.1021/la981608c>
- Gomez-Suarez, C., Noordmans, J., van der Mei, H. C., & Busscher, H. J. (2001). Air bubble induced detachment of polystyrene particles with different sizes from collector surfaces in a parallel plate flow chamber. *Colloids & Surface*, 186(3), 211–219. [https://doi.org/10.1016/s0927-7757\(00\)00799-8](https://doi.org/10.1016/s0927-7757(00)00799-8)
- Gomez-Suarez, C., van der Mei, H. C., & Busscher, H. J. (2000). Air bubble-induced detachment of positively and negatively charged polystyrene particles from collector surfaces in a parallel-plate flow chamber. *Journal of Adhesion Science and Technology*, 14(12), 1527–1537. <https://doi.org/10.1163/156856100742357>
- Grillo, R., Rosa, A. H., & Fraceto, L. F. (2015). Engineered nanoparticles and organic matter: A review of the state-of-the-art. *Chemosphere*, 119, 608–619. <https://doi.org/10.1016/j.chemosphere.2014.07.049>
- Ishida, N. (2007). Direct measurement of hydrophobic particle-bubble interactions in aqueous solutions by atomic force microscopy: Effect of particle hydrophobicity. *Colloids and Surfaces A: Physicochemical and Engineering Aspects*, 300(3), 293–299. <https://doi.org/10.1016/j.colsurfa.2007.02.003>
- Kaplan, D. I., Bertsch, P. M., Adriano, D. C., & Miller, W. P. (1993). Soil-borne mobile colloids as influenced by water flow and organic carbon. *Environmental Science & Technology*, 27(6), 1193–1200. <https://doi.org/10.1021/es00043a021>
- Kessler, R. (2011). Engineered nanoparticles in consumer products: Understanding a new ingredient. *Environmental Health Perspectives*, 119(3), a120–a125. <https://doi.org/10.1289/ehp.119-a120>
- Khan, S., Naushad, M., Al-Gheethi, A., & Iqbal, J. (2021). Engineered nanoparticles for removal of pollutants from wastewater: Current status and future prospects of nanotechnology for remediation strategies. *Journal of Environmental Chemical Engineering*, 9(5), 106160. <https://doi.org/10.1016/j.jece.2021.106160>
- Knappenberger, T., Flury, M., Mattson, E. D., & Harsh, J. B. (2014). Does water content or flow rate control colloid transport in unsaturated porous media? *Environmental Science & Technology*, 48(7), 3791–3799. <https://doi.org/10.1021/es404705d>
- Kralchevsky, P., & Nagayama, K. (2001). Particles at fluid interfaces and membranes. In *Attachment of colloid particles and proteins to interfaces and formation of two-dimensional arrays*. Elsevier.
- Krishna, Y. S. R., & Seetha, N. (2022). Predicting the rate coefficients of attachment and detachment of colloids in saturated porous media. *Frontiers in Water*, 4, 1–18. <https://doi.org/10.3389/frwa.2022.827923>
- Lazouskaya, V., & Jin, Y. (2008). Colloid retention at air water interface in a capillary channel. *Colloids and Surfaces A: Physicochemical and Engineering Aspects*, 325(3), 141–151. <https://doi.org/10.1016/j.colsurfa.2008.04.053>
- Lemelle, L., Paliere, J. F., Chatre, E., & Place, C. (2010). Counterclockwise circular motion of bacteria swimming at the air-liquid interface. *Journal of Bacteriology*, 192(23), 6307–6308. <https://doi.org/10.1128/jb.00397-10>
- Lenhart, J. J., & Saiers, J. E. (2002). Transport of silica colloids through unsaturated porous media: Experimental results and model comparisons. *Environmental Science & Technology*, 36(4), 769–777. <https://doi.org/10.1021/es0109949>
- Li, X., Scheibe, T. D., & Johnson, W. P. (2004). Apparent decreases in colloid deposition rate coefficient with distance of transport under unfavourable deposition conditions: A general phenomenon. *Environmental Science & Technology*, 38(21), 5616–5625. <https://doi.org/10.1021/es049154v>
- Li, X., Zhang, P., Lin, C. L., & Johnson, W. P. (2005). Role of hydrodynamic drag on microsphere deposition and re-entrainment in porous media under unfavourable conditions. *Environmental Science & Technology*, 39(11), 4012–4020. <https://doi.org/10.1021/es048814t>
- Lin, D., Hu, L., Bradford, S. A., Zhang, X., & Lo, I. M. (2021). Simulation of colloid transport and retention using a pore-network model with roughness and chemical heterogeneity on pore surfaces. *Water Resources Research*, 57(2), e2020WR028571. <https://doi.org/10.1029/2020wr028571>
- Lin, D., Zhang, X., Hu, L., Bradford, S. A., & Shen, C. (2022). Prediction of colloid sticking efficiency at pore-scale and macroscale using a pore network model. *Journal of Hydrology*, 612, 128253. <https://doi.org/10.1016/j.jhydrol.2022.128253>
- Logan, B. E., Jewett, D. G., Arnold, R. G., Bower, E. J., & O'Melia, C. R. (1995). Clarification of clean-bed filtration models. *Journal of Environmental Engineering*, 121(12), 869–873. [https://doi.org/10.1061/\(asce\)0733-9372\(1995\)121:12\(869\)](https://doi.org/10.1061/(asce)0733-9372(1995)121:12(869))
- Manoharan, V. N. (2015). Colloids at interfaces: Pinned down. *Nature Materials*, 14(9), 869–870. <https://doi.org/10.1038/nmat4400>
- Mitropoulou, P. N., Syngouna, V. I., & Chrysikopoulos, C. V. (2013). Transport of colloids in unsaturated packed columns: Role of ionic strength and sand grain size. *Environmental Science & Technology*, 47, 2153–2160. <https://doi.org/10.1016/j.cej.2013.07.093>
- Park, C. M., Heo, J., Her, N., Chu, K. H., Jang, M., & Yoon, Y. (2016). Modeling the effects of surfactant, hardness, and natural organic matter on deposition and mobility of silver nanoparticles in saturated porous media. *Water Research*, 103, 38–47. <https://doi.org/10.1016/j.watres.2016.07.022>
- Park, Y., Atwill, E. R., Ho, L., Packman, A. I., & Harter, T. (2012). Deposition of *Cryptosporidium parvum* oocysts in porous media: A synthesis of attachment efficiencies measured under varying environmental conditions. *Environmental Science & Technology*, 46(17), 9491–9500. <https://doi.org/10.1021/es300564w>
- Patzek, T. (2000). Verification of a complete pore network simulator of drainage and imbibition. *Society of Petroleum Engineers Journal*, 6(2), 144–156. <https://doi.org/10.2118/71310-pa>
- Patzek, T. W., & Kristensen, J. G. (2001). Shape factor correlations of hydraulic conductance in noncircular capillaries II. Two-phase creeping flow. *Journal of Colloid and Interface Science*, 236(2), 305–317. <https://doi.org/10.1006/jcis.2000.7414>
- Qi, Z., Zhang, L., Wang, F., Hou, L., & Chen, W. (2014). Factors controlling transport of graphene oxide nanoparticles in saturated sand columns. *Environmental Toxicology and Chemistry*, 33(5), 998–1004. <https://doi.org/10.1002/etc.2525>
- Radeov, B., Nedyalkov, M., & Dyakovich, V. (1992). Brownian motion at liquid-gas interfaces. 1. Diffusion coefficients of macroparticles at pure interfaces. *Langmuir*, 8(12), 2962–2965. <https://doi.org/10.1021/la00048a019>
- Redman, J. A., Grant, S. B., Olson, T. M., & Estes, M. K. (2001). Pathogen filtration, heterogeneity, and the potable reuse of wastewater. *Environmental Science & Technology*, 35(9), 1798–1805. <https://doi.org/10.1021/es010960>
- Ruckenstein, E., & Prieve, D. C. (1973). Rate of deposition of Brownian particles under the action of London and double-layer Forces. *Journal of the Chemical Society, Faraday Transactions*, 2(69), 1522–1536. <https://doi.org/10.1039/f29736901522>
- Rudramurthy, G. R., & Swamy, M. K. (2018). Potential applications of engineered nanoparticles in medicine and biology: An update. *Journal of Biological Inorganic Chemistry*, 23(8), 1185–1204. <https://doi.org/10.1007/s00775-018-1600-6>
- Ryan, J. N., Illangasekare, T. H., Litaor, M. I., & Shannon, R. (1998). Particle and plutonium mobilization in macroporous soils during rainfall simulations. *Environmental Science & Technology*, 32(4), 476–482. <https://doi.org/10.1021/es970339u>

- Sadeghi, G., Schijven, J. F., Behrends, T., Hassanizadeh, S. M., Gerrits, J., & Kleingeld, P. J. (2011). Systematic study of effects of pH and ionic strength on attachment of phage PRD1. *Ground Water*, 49(1), 12–19. <https://doi.org/10.1111/j.1745-6584.2010.00767.x>
- Saiers, J. E., Hornberger, G. M., Gower, D. B., & Herman, J. S. (2003). The role of moving air–water interfaces in colloid mobilization within the vadose zone. *Geophysical Research Letters*, 30(21), 2083. <https://doi.org/10.1029/2003GL018418>
- Saiers, J. E., & Lenhart, J. J. (2003). Colloid mobilization and transport within unsaturated porous media under transient-flow conditions. *Water Resources Research*, 39(1), 1019. <https://doi.org/10.1029/2002WR001370>
- Sang, W., Morales, V. L., Zhang, W., Stooft, C. R., Bao, B., Schatz, A. L., et al. (2013). Quantification of colloid retention and release by straining and energy minima in variably saturated porous media. *Environmental Science & Technology*, 47, 8256–8264. <https://doi.org/10.1021/es400288c>
- Schafer, A., Harms, H., & Zehnder, A. J. B. (1998). Bacterial accumulation at the air–water interface. *Environmental Science & Technology*, 32(23), 3704–3712. <https://doi.org/10.1021/es980191u>
- Schafer, A., Ustohal, P., Harms, H., Stauff er, F., Dracos, T., & Zehnder, A. J. B. (1998). Transport of bacteria in unsaturated porous media. *Journal of Contaminant Hydrology*, 33(1–2), 149–169. [https://doi.org/10.1016/s0169-7722\(98\)00069-2](https://doi.org/10.1016/s0169-7722(98)00069-2)
- Schijven, J. F., & Hassanizadeh, S. M. (2000). Removal of viruses by soil passage: Overview of modeling, processes, and parameters. *Critical Reviews in Environmental Science and Technology*, 30(1), 49–127. <https://doi.org/10.1080/10643380091184174>
- Seetha, N., Majid Hassanizadeh, S., Mohan Kumar, M. S., & Raof, A. (2015). Correlation equations for average deposition rate coefficients of nanoparticles in a cylindrical pore. *Water Resources Research*, 51(10), 8034–8059. <https://doi.org/10.1002/2015WR017723>
- Seetha, N., Mohan Kumar, M. S., Hassanizadeh, S. M., & Raof, A. (2014). Virus-sized colloid transport in a single pore: Model development and sensitivity analysis. *Journal of Contaminant Hydrology*, 164, 163–180. <https://doi.org/10.1016/j.jconhyd.2014.05.010>
- Seetha, N., Raof, A., Mohan Kumar, M. S., & Majid Hassanizadeh, S. (2017). Upscaling of nanoparticle transport in porous media under unfavourable conditions: Pore scale to Darcy scale. *Journal of Contaminant Hydrology*, 200, 1–14. <https://doi.org/10.1016/j.jconhyd.2017.03.002>
- Shang, J., Flury, M., Chen, G., & Zhuang, J. (2008). Impact of flow rate, water content, and capillary forces on in situ colloid mobilization during infiltration in unsaturated sediments. *Water Resources Research*, 44(6), W06411. <https://doi.org/10.1029/2007WR006516>
- Sharma, P., Flury, M., & Zhou, J. (2008). Detachment of colloids from a solid surface by a moving air–water interface. *Journal of Colloid and Interface Science*, 326(1), 143–150. <https://doi.org/10.1016/j.jcis.2008.07.030>
- Sirivithayapakorn, S., & Keller, A. (2003). Transport of colloids in unsaturated porous media: A pore-scale observation of processes during the dissolution of air–water interface. *Water Resources Research*, 39(12), 1346. <https://doi.org/10.1029/2003WR002487>
- Spielman, L. A., & Friedlander, S. K. (1974). Role of the electrical double layer in particle deposition by convective diffusion. *Journal of Colloid and Interface Science*, 46(1), 22–31. [https://doi.org/10.1016/0021-9797\(74\)90021-6](https://doi.org/10.1016/0021-9797(74)90021-6)
- Steenhuis, T. S., Dathe, A., Zevi, Y., Smith, J. L., Gao, B., Shaw, S. B., et al. (2006). Biocolloid retention in partially saturated soils. *Biologia*, 61(S19), S229–S233. <https://doi.org/10.2478/s11756-006-0163-0>
- Stocco, A., Chollet, B., Wang, X., Blanc, C., & Nobili, M. (2019). Rotational diffusion of partially wetted colloids at fluid interfaces. *Journal of Colloid and Interface Science*, 542, 363–369. <https://doi.org/10.1016/j.jcis.2019.02.017>
- Tan, S. Y., Whitby, C. P., Ralston, J., & Fornasiero, D. (2009). Brownian diffusion of ultrafine particles to an air–water interface. *Advanced Powder Technology*, 20(3), 262–266. <https://doi.org/10.1016/j.apt.2009.03.001>
- Tong, M., Li, X., Brow, C. N., & Johnson, W. P. (2005). Detachment-influenced transport of an adhesion-deficient bacterial strain within water-reactive porous media. *Environmental Science & Technology*, 39(8), 2500–2508. <https://doi.org/10.1021/es049013t>
- Torkzaban, S., Bradford, S. A., van Genuchten, M. T., & Walker, S. L. (2008). Colloid transport in unsaturated porous media: The role of water content and ionic strength on particle straining. *Journal of Contaminant Hydrology*, 96(1–4), 113–127. <https://doi.org/10.1016/j.jconhyd.2007.10.006>
- Torkzaban, S., Hassanizadeh, S. M., Schijven, J. F., & van den Berg, H. H. J. L. (2006). Role of air–water interfaces on retention of viruses under unsaturated conditions. *Water Resources Research*, 42(12), W12S14. <https://doi.org/10.1029/2006WR004904>
- Toro-Mendoza, J., Rodríguez-Lopez, G., & Paredes-Altuve, O. (2017). Brownian diffusion of a particle at an air/liquid interface: The elastic (not viscous) response of the surface. *Physical Chemistry Chemical Physics*, 19(13), 9092–9095. <https://doi.org/10.1039/c6cp07442a>
- Tufenkji, N., & Elimelech, M. (2004). Correlation equation for predicting single-collector efficiency in physiochemical filtration in saturated porous media. *Environmental Science & Technology*, 38(2), 529–536. <https://doi.org/10.1021/es034049r>
- Van Oss, C. J. (2006). *Interfacial forces in aqueous media* (2nd ed.). CRC Press.
- Wan, J., & Tokunaga, T. K. (1997). Film straining of colloids in unsaturated porous media: Conceptual model and experimental testing. *Environmental Science & Technology*, 31(8), 2413–2420. <https://doi.org/10.1021/es970017q>
- Wan, J. M., & Wilson, J. L. (1994). Colloid transport in unsaturated porous media. *Water Resources Research*, 30(4), 857–864. <https://doi.org/10.1029/93wr03017>
- Wan, J. M., Wilson, J. L., & Kieft, T. L. (1994). Influence of the gas–water interface on transport of microorganisms through unsaturated porous media. *Applied and Environmental Microbiology*, 60(2), 509–516. <https://doi.org/10.1128/aem.60.2.509-516.1994>
- Wang, M., Gao, B., Tang, D., Sun, H., Yin, X., & Yu, C. (2017). Effects of temperature on graphene oxide deposition and transport in saturated porous media. *Journal of Hazardous Materials*, 331, 28–35. <https://doi.org/10.1016/j.jhazmat.2017.02.014>
- Williams, D. F., & Berg, J. C. (1992). The aggregation of colloidal particles at the air–water interface. *Journal of Colloid and Interface Science*, 152(1), 218–229. [https://doi.org/10.1016/0021-9797\(92\)90021-d](https://doi.org/10.1016/0021-9797(92)90021-d)
- Xu, S., Qi, J., Chen, X., Lazouskaya, V., Zhuang, J., & Jin, Y. (2016). Coupled effect of extended DLVO and capillary interactions on the retention and transport of colloids through unsaturated porous media. *Science of the Total Environment*, 573, 564–572. <https://doi.org/10.1016/j.scitotenv.2016.08.112>
- Yao, K. M., Habibian, M. T., & O'Melia, C. R. (1971). Water and waste water filtration: Concepts and applications. *Environmental Science & Technology*, 5(11), 1105–1112. <https://doi.org/10.1021/es60058a005>
- Zevi, Y., Dathe, A., Gao, B., Zhang, W., Richards, B. K., & Steenhuis, T. S. (2009). Transport and retention of colloidal particles in partially saturated porous media: Effect of ionic strength. *Water Resources Research*, 45(12), W12403. <https://doi.org/10.1029/2008WR007322>
- Zevi, Y., Dathe, A., McCarthy, J. F., Richards, B. K., & Steenhuis, T. S. (2005). Distribution of colloid particles onto interfaces in partially saturated sand. *Environmental Science & Technology*, 39(18), 7055–7064. <https://doi.org/10.1021/es048595b>
- Zevi, Y., Gao, B., Zhang, W., Morales, V. L., Cakmak, M. E., Medrano, E. A., et al. (2012). Colloid retention at the meniscus–wall contact line in an open microchannel. *Water Research*, 46(2), 295–306. <https://doi.org/10.1016/j.watres.2011.09.046>
- Zhang, Q., Hassanizadeh, S. M., Karadimitriou, N. K., Raof, A., Liu, B., Kleingeld, P. J., & Imhof, A. (2013). Retention and remobilization of colloids during steady-state and transient two-phase flow. *Water Resources Research*, 49(12), 8005–8016. <https://doi.org/10.1002/2013WR014345>

- Zhang, Q., Hassanizadeh, S. M., Liu, B., Schijven, J. F., & Karadimitriou, N. K. (2014). Effect of hydrophobicity on colloid transport during two-phase flow in a microchannel. *Water Resources Research*, *50*(10), 7677–7691. <https://doi.org/10.1002/2013WR015198>
- Zhuang, J., McCarthy, J. F., Tyner, J. S., Perfect, E., & Flury, M. (2007). In-situ colloid mobilization in Hanford sediments under unsaturated transient flow conditions: Effect of irrigation pattern. *Environmental Science & Technology*, *41*(9), 3199–3204. <https://doi.org/10.1021/es062757h>
- Zhuang, J., Qi, J., & Jin, Y. (2005). Retention and transport of amphiphilic colloids under unsaturated flow conditions: Effect of particle size and surface property. *Environmental Science & Technology*, *39*(20), 7853–7859. <https://doi.org/10.1021/es050265j>